國立臺灣大學理學院物理學研究所

碩士論文

Department of Physics

College of Science

National Taiwan University

Master Thesis

奈米晶矽方塊之光熱效應致雙穩態散射

Photothermal Bistability Scattering in a Single Crystalline Silicon Nanoblock

陳育傑

Yu-Chien Chen

指導教授：朱士維 博士

Advisor: Shi-Wei Chu, Ph.D.

中華民國 112 年 1 月

January 2023

doi:10.6342/NTU202301642

口試委員會審定書

國立臺灣大學碩士學位論文
口試委員會審定書

奈米晶矽方塊之光熱效應致雙穩態散射
Photothermal Bistability Scattering in a Single Crystalline Silicon Nanoblock

本論文係陳育傑君（R09222021）在國立臺灣大學物理學所完成之碩士學位論文，於民國 112 年 1 月 13 日承下列考試委員審查通過及口試及格，特此證明

口試委員：朱士維（簽名）

（指導教授）張之威　易富萍

陳國平

doi:10.6342/NTU202301642

致謝

在實驗室三年的研究生涯中，從光路的架設到 COMSOL 模擬，過程中得到很多人的協助，我要向在我研究生涯協助我的每一位表示感謝。

首先，我要謝謝指導教授朱士維教授，非常感激您的悉心指導和寶貴建議，尤其是您強調的報告與研究的嚴謹邏輯，影響我深遠，此外您的耐心和鼓勵則激發了我持續努力完成這份研究。

再來我想要感謝來自 ITMO 的 Mihail Petrov 教授，感謝您提供了許多關於模擬的寶貴建議和物理理論的討論。您模擬的專業知識和深入見解對我在建立雷射加熱模型方面起到了重要的幫助。感謝張之威老師和林宮玄老師，每次的會議討論給予許多不同方面的研究建議並激發了我新的思考，感謝大阪大學的高原淳一教授以及 Shin-Etsu Silicone 公司提供實驗樣品。

接著我要謝謝實驗室大家的幫忙，他們在我研究生涯中給予了我許多的幫助。謝謝邦漢學長帶領我學習如何調整光路以及架設光路，謝謝毓隆學長手把手教我 COMSOL 模擬，非常有耐心地回答我所有模擬上的問題，引領我進入數值模擬的領域並獲得準確的結果，謝謝德心學長，提供了實驗數據，驗證了模擬的準確性，我們一起討論並且證明了矽奈米方塊的雙穩態現象，對於本研究功不可沒，感謝西田健太郎和 Mor Pal 給予本研究許多建議，感謝柏學、荐軒和學弟妹們，和大家一起的討論和成長是我研究生涯中的寶貴且快樂的時光。

感謝家人無私奉獻和支持，無論是在生活還是在學業上，讓我相信自己能夠克服一切困難。

doi:10.6342/NTU202301642

中文摘要

雙穩態系統在生活中十分的常見，特別是在數位電路中的正反電路。正反電路是電子產品中最主要的元件之一，藉由產生 0 與 1 兩個穩定態來儲存二進位數位資料。近幾十年來，光學雙穩態越來越受到關注，因為它提供了高速光學正反電路可以解決電子電路調制時間較慢的問題，此外也有許多其他應用，例如光儲存器等等。光學雙穩態的組成條件為共振腔以及非線性介質，在所有的非線性材料中，矽基光學雙穩態備受關注，基於矽在現今的製程上有具有較高相容性和高折射率的特性，能夠有更強的光限制性，然而矽材料自身的非線性較小(10^{-9}微米平方每毫瓦)，因此藉由提升共振腔的品質因子來增強光學雙穩態的非線性響應，為了提升品質因子，矽共振腔的大小通常在微米的大小，這對於光積體電路來說是個缺點。最近我們結合光熱效應與米氏共振設計出低品質因子奈米方塊共振腔，並將非線性折射率提高到 10^{-1}微米平方每毫瓦，這有效的提高了光學的非線性，因此我們利用同樣的概念，利用低品質因子奈米方塊共振腔達到光熱效應雙穩態。

在本研究中，藉由驗證過的模擬模型在特定的雷射光波長之下模擬激發強度依賴性並預測哪種尺寸的奈米方塊具有光熱效應雙穩態，此外我們針對具有光熱效應雙穩態的奈米結構，利用數值模擬，證明光熱效應雙穩態同時會伴隨著遲滯效應。為了能夠證明光熱效應雙穩態普遍存在於矽奈米結構中，我們藉由數值模擬，藉由調整雷射光波長，使得原本沒有光學雙穩態現象的奈米結構，也有光學雙穩態，證明了光熱效應雙穩態的普遍性。除此之外，我們模擬雷射掃描影像，並提出超解析的應用。最後我們用測量結果證明了光熱雙穩態的預測。我們的研究設計出目前尺寸以及品質因子皆最小的雙穩態共振結構。

關鍵字: 光學雙穩態、矽光子學、光熱效應雙穩態、有限元素法、解析度提升

doi:10.6342/NTU202301642

Abstract

Bistability is commonly used in electronics flip-flop circuits. It generates two stable states to store binary digital information. In recent decades, optical bistability becomes popular, because it offers optical flip flops leading to applications such as optical memory. Optical bistability is composed of a resonator and a nonlinear medium. Silicon-based optical bistability has drawn much attention among all kinds of nonlinear mediums. Since silicon has stronger light confinement. However, the intrinsic Kerr nonlinearity of silicon n_2 is $10^{-9}\ \mu m^2/mW$. We need high Q resonators to enhance the nonlinear response of optical bistability. We recently discovered that the Mie-enhanced photothermal effect in a low Q factor resonator increases the nonlinear refractive index up to $10^{-1}\ \mu m^2/mW$. Therefore, we can achieve photothermal bistability in a low Q-factor silicon resonator.

In this work, we use a validated numerical simulation model to simulate the excitation intensity dependence under certain laser wavelengths and predict which size of the particle has photothermal bistability. In addition, we have conducted a validated simulation model to demonstrate that photothermal bistability is accompanied by hysteresis effects. To show the generality of photothermal bistability, we conducted numerical simulations. By adjusting the wavelength of the laser light, we can induce optical bistability in nanostructures that originally did not exhibit such behavior. This provided evidence that photothermal bistability can be observed in nanostructures of different sizes under different laser light wavelengths. Moreover, we simulate the laser scanning images and provide a possible application of super-resolution enhancement. Last but not least, we offer a preliminary experimental result to demonstrate the existence of photothermal bistability in silicon nanostructures. Our study designs a bistable nanostructure with the smallest size and Q factor so far.

Keywords: optical bistability, photothermal bistability, finite element method, silicon photonics, resolution enhancement

doi:10.6342/NTU202301642

Contents

doi:10.6342/NTU202301642

Figure list

doi:10.6342/NTU202301642

Table list

doi:10.6342/NTU202301642

Chapter 1 Introduction

The phenomenon of bistability is common in our life, especially in digital electronics. In digital electronics, bistability is crucial in flip-flop circuits which are the fundamental component for computers and communications. It contains transistors which are nonlinear electronic devices to form feedback loops to generate two stable states: 1 and 0. Therefore, it can store binary digital information. However, there are some limitations in digital electronics, such as energy loss and modulation speed. In recent years, nanophotonics with optical bistability has drawn great attention because it provides optical switches and optical flip flop [1-3] which lift the limitations in digital electronics. Besides, optical bistability has a characteristic of large state transition in excitation dependence, and the slope of the transition has been theoretically proven to approach infinity[4] which enables many other applications, including lasing, modulation, and optical memory [5-7].

Similar to bistable electronics, the typical system of optical bistability is composed of an input-dependent nonlinear medium and a feedback loop to create two stable states[8]. Several materials have been published that can be the nonlinear medium for optical bistability devices, including TiO_2, graphene, silicon, etc.[9-11]. Among them, silicon is the favored material because of its compatibility with modern industry lines and its natural abundance. In addition, since silicon has high refractive index, it has strong light confinement and lower non-radiative losses than metals [12-14]. Therefore, silicon-based optical bistability devices have become popular and have many applications [15-17]. However, these devices require high Q resonators, such as ring resonators with Q factor higher than 10^3, to compensate for the weak intrinsic n_2 Kerr nonlinearity of silicon(10^{-9} $\mu m^2/mW$)[18]. The photothermal effect is a nonlinear effect that provides

doi:10.6342/NTU202301642

a higher nonlinear refractive index up to $10^{-6}\ \mu m^2/mW$[19]. Nevertheless, we still need a high Q resonator: Quasi-BIC nanoresonator to increase the optical response[20]. Furthermore, the size of the high Q resonator is often in micrometer scale which is a disadvantage to designing high-density photonics circuits [15-17].

To increase the optical response of the device, we can enhance the light-matter interaction by the Mie resonance modes with nanometer-scale silicon structures [21]. Recently, our studies show that by combining the photothermal effect with Mie resonance, the nonlinear refractive index can be increased up to $10^{-1}\ \mu m^2/mW$. This represents a notable increase of five orders of magnitude compared to the nonlinear optical index of the bulk photothermal effect[22, 23]. Furthermore, the Mie-enhanced silicon resonator exhibits a Q-factor of approximately 10, which is at least two orders of magnitude lower than high-Q structures. Therefore, this large nonlinearity should relax the requirement of high Q resonators for optical bistability. Since the nonlinearity comes from the photothermal effect, we named it photothermal bistability.

In this work, we establish the numerical simulation model to demonstrate photothermal bistability in a single crystal silicon nanoblock with a volume size around $10^{-3}\ \mu m^3$. With the simulation model, we find out that the mechanism of photothermal bistability can be explained by the nonlinearity of the temperature-dependent absorption. We provide the experimental results by laser scanning microscopy to prove the existence of photothermal bistability in silicon nanoblock. In **Chapter 2**, we discuss theories of the photothermal effect and optical bistability. In **Chapter 3**, we show the details of two laser heating simulations which are separate model and combination model. Besides, we show the setup of laser scanning microscopy and the sample fabrication. In **Chapter 4**, we demonstrate the simulation results and experimental results of photothermal bistability and give a possible application of super resolution. Our study

doi:10.6342/NTU202301642

provides a guideline for designing a bistable system with a single crystal silicon nanoblock.

doi:10.6342/NTU202301642

Chapter 2 Theory

This chapter explains the theories of this research, including Mie-enhanced nonlinearity, and optical bistability.

2.1 Mie Enhanced Nonlinearity

In this section, we will introduce Mie scattering, which occurs when light interacts with particles of similar size to its wavelength. Besides its scattering properties, Mie scattering has garnered interest for its ability to enhance nonlinear effects. We will discuss the details in the following sections.

2.1.1 Mie Scattering

Mie scattering takes place when the dimensions of the scatterer are on a similar scale as the wavelength of the electromagnetic wave. This phenomenon is proposed by Dr. Gustav Mie in 1908[24]. The scattering fields of Mie scattering are linear combinations of Mie resonance modes. And the Mie resonance modes can be defined by the displacement current in the scatterer. For instance, when the scatterer's displacement current is linear, the electric dipole mode will be excited. Similarly, when the scatterer's displacement current forms a circular loop, the magnetic dipole mode will be excited. When the scatterer's displacement current becomes more complex, the higher Mie resonance modes, such as electric quadrupole and magnetic quadrupole, may be excited. Since the interference between the excited resonance modes will cause different optical responses, the optical responses of the scatterer will rely on the optical properties and the geometry of the scatterer. Therefore, with the well-designed Mie resonator, there will be a lot of applications, such as nanoantennas[25], high Q structure[26, 27], all-optical modulator[22], and perfect absorber [28]. Next, we want to show some crucial formulas

doi:10.6342/NTU202301642

of Mie scattering.

The optical response of the nanostructure with a light source can be quantified by cross-section. The formula of absorption cross-section C_{abs}, scattering cross-section C_{sca}, extinction cross-section C_{ext} are shown below[29].

$$C_{sca} = \frac{2\pi}{k^2}\sum_{n}^{\infty}(2n+1)(|a_n|^2 + |b_n|^2) \quad (2.1.1.1)$$

$$C_{ext} = \frac{2\pi}{k^2}\sum_{n}^{\infty}(2n+1)Re(a_n + b_n) \quad (2.1.1.2)$$

$$C_{abs} = C_{ext} - C_{sca} \quad (2.1.1.3)$$

Where *k* is the wavenumber, n is the quantized orbital angular momentum, a_n is the Mie coefficient corresponding to the electric mode, and b_n is the Mie coefficient corresponding to the magnetic mode. The subscript of a_n and b_n is the degree of the mode. For instance, *n*=1 is the dipole mode and *n*=2 is the quadrupole. As the results, we can derive the scattering cross-section of the first four modes from **Eq.2.1.1.1** as shown below.

$$C_{sca,ED} = \frac{6\pi}{k^2}|a_1|^2 \quad (2.1.1.4)$$

$$C_{sca,MD} = \frac{6\pi}{k^2}|b_1|^2 \quad (2.1.1.5)$$

$$C_{sca,EQ} = \frac{10\pi}{k^2}|a_2|^2 \quad (2.1.1.6)$$

$$C_{sca,MQ} = \frac{10\pi}{k^2}|b_2|^2 \quad (2.1.1.7)$$

The subscript of the scattering cross-section indicates the corresponding scattering mechanisms: electric dipole, magnetic dipole, electric quadrupole, and magnetic quadrupole. **Fig. 2.1.1** is an example of the multipole decomposition of Mie scattering. The first peak is associated with the electric dipole, while the second peak is associated with the magnetic dipole.

doi:10.6342/NTU202301642

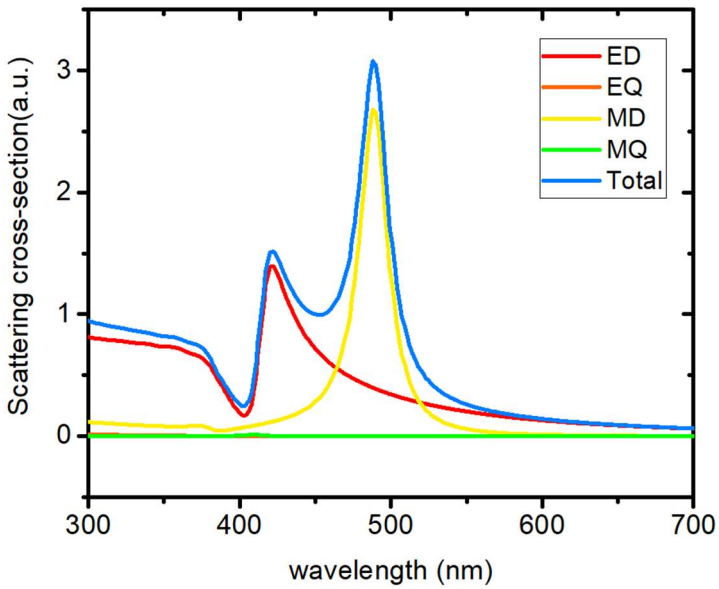

Figure 2.1.1: The scattering spectrum of 110 nm silicon nanosphere.

The refractive index is measured by ellipsometry[22]. The blue line is the total scattering cross-section. The red and orange lines correspond to the scattering cross-section of an electric dipole and electric quadrupole. The yellow and green lines correspond to the scattering cross-section of magnetic dipole, and magnetic quadrupole. This calculation was conducted by *PyMieScatt*[30].

As **Fig. 2.1.1** shows, we know that the Mie resonance mode will be affected by the refractive index and particle size. **Fig. 2.1.2** is the scattering efficiency spectral map with different refractive indices and diameters of the particle. The scattering efficiency is $Q_{sca} = C_{sca}/\pi r^2$, where r indicates the particle's radius. We can observe that the peak in the spectrum exhibit redshift when the particle size or the refractive index increase.

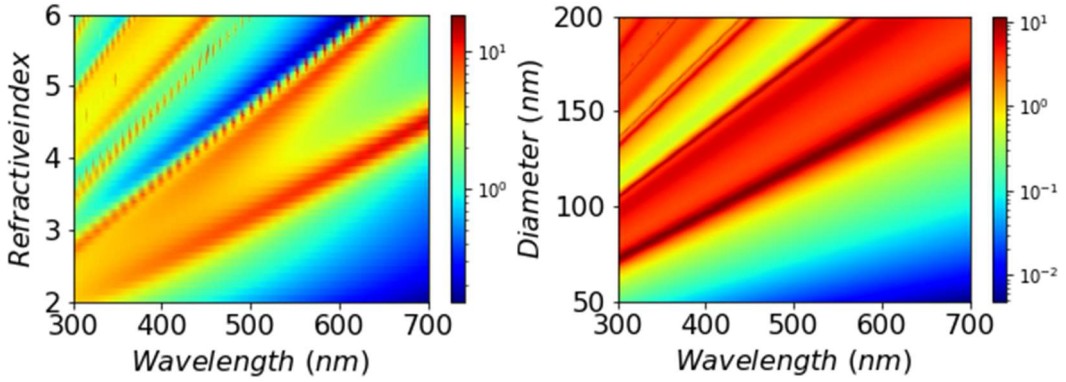

Figure 2.1.2: The Mie scattering efficiency spectra

(a) different refractive index with a fixed diameter at 110 nm (b) different diameters with a fixed refractive index at 4. This calculation was conducted by *PyMieScatt*[30].

From the discussion above, we learn that we can design the desired Mie resonator

doi:10.6342/NTU202301642

by tuning the refractive index and the diameter of the particle. However, the analytical solution is only available for spheres. Therefore, for other shapes of the particle, we need numerical simulation to calculate the Mie scattering. In **Section 3.3**, we will discuss the theory of the finite element method (FEM).

2.1.2 Kerr Nonlinearity and Photo-thermo-optical Nonlinearity

It is crucial to induce the nonlinearity of the Mie resonator for application, such as all-optical modulator[5]. In **Section 2.1.1**, we know that the refractive index and particle size affect the Mie resonance mode of the particle. For an established nanostructure, one of the ways to tune the refractive index is Kerr nonlinearity. By changing the applied electric field, the refractive index will change. To illustrate the interplay of the applied electric field and the material, we utilize the polarization density P. In the linear case, the polarization density is shown below[31].

$$P = \varepsilon_0 \chi_e E \qquad (2.1.2.1)$$

Where χ_e denotes the electric susceptibility, ε_0 denotes the vacuum permittivity, and E is the applied electric field. **Eq. 2.1.2.1** shows that the polarization density is directly related to the electric field. However, it only applies when the electric field is weak. During a strong electric field, the connection between the electric field and the polarization density exhibits nonlinearity.

$$P = \varepsilon_0[\chi^{(1)}E + \chi^{(2)}E^2 + \chi^{(3)}E^3 + \cdots] \qquad (2.1.2.2)$$

where $\chi^{(n)}$ is the nth-order electric susceptibility. Eq.2.1.2.2 shows that higher-order susceptibility becomes important when the electric field gets stronger. In this study, we

doi:10.6342/NTU202301642

use silicon as our material. Since silicon is a centrosymmetric crystal, $\chi^{(2)}$ can be omitted. We can derive the general form of the refractive index from **Eq. 2.1.2.2[31]**.

$$n = n_0 + n_2 I - i\frac{\lambda}{4\pi}(\alpha_0 + \alpha_2 I) \quad (2.1.2.3)$$

where I is the electric field intensity, λ denotes the electric field wavelength, α_0 denotes the linear absorption coefficient, α_2 denotes the nonlinear absorption coefficient, n_2 denotes the Kerr nonlinear refractive index coefficient, and n_0 denotes the linear refractive index.

$$n_2 = \frac{3}{4c{n_0}^2\varepsilon_0} Re(\chi^{(3)}) \quad (2.1.2.4)$$

$$\alpha_2 = -\frac{3\omega}{2c^2{n_0}^2\varepsilon_0} Im(\chi^{(3)}) \quad (2.1.2.5)$$

From **Eq. 2.1.2.3**, we can tune the refractive index by changing the intensity of the electric field. For silicon, the Kerr nonlinearity n_2 is around $10^{-9}\ \mu m^2/mW$ [31]. Therefore, to get 10% of the refractive index modulation, the field intensity will be $10^8\ mW/\mu m^2$ which can easily cause damage to the nanostructure.

Except for Kerr nonlinearity, the photo-thermo-optical effect can also cause the refractive index change. The mechanisms causing these two nonlinear refractive indices are different. The mechanism of the photo-thermo-optical effect contains two processes called self-induced optical heating[32] shown in **Fig 2.1.3**. The first process is the photothermal effect. When the light source impinges on the material, the material absorbs the energy based on the absorption cross-section induced by Mie resonance. As a result, the temperature increases. The second and third process is the thermo-optical effect. Since the material's refractive index is temperature-dependent, the absorption cross-section also changes with temperature. These two processes continue until the temperature comes to equilibrium.

doi:10.6342/NTU202301642

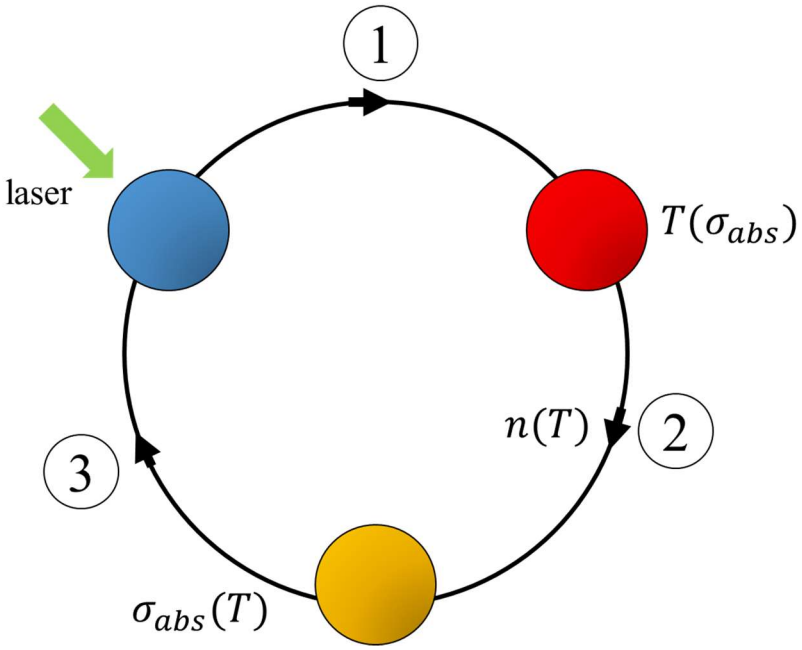

Figure 2.1.3 Mechanism of self-induced optical heating.

Circle 1 denotes the process of the photothermal effect. Circle 2 denotes the process of the refractive index change by temperature. Circle 3 denotes the process of the absorption cross section changed by the refractive index. Circle 2 and circle 3 together represent the process of thermo-optical effect.

The derivation of photo-thermo-optical nonlinearity-induced refractive index change is shown below. The relation of the temperature and the refractive index is,

$$n = n_0 + \frac{dn}{dT}\Delta T \qquad (2.1.2.6)$$

Where $\frac{dn}{dT}$ is the temperature coefficient, ΔT is the temperature rise of the material caused by the light source. The temperature rise can be computed through the heat equation.

$$\rho C_p \frac{\partial \Delta T}{\partial t} - \kappa \nabla^2(\Delta T) = \alpha I \qquad (2.1.2.7)$$

Where C_p represnts the heat capacity, ρ denotes the density, κ denotes the thermal conductivity, α is the absorption coefficient, and I represents the intensity of the light source. When the temperature reaches equilibrium, we can ignore the first term in **Eq. 2.1.2.7**.

$$-\kappa \nabla^2(\Delta T) = \alpha I \qquad (2.1.2.8)$$

doi:10.6342/NTU202301642

Furthermore, taking into account the temperature within the region encompassing a radius of r, and r represents the radius of the light source. We can rewrite **Eq.2.1.2.8** as below.

$$\Delta T = \frac{\alpha I r^2}{\kappa} \tag{2.1.2.9}$$

Replacing **Eq.2.1.2.9** into **Eq.2.1.2.6**, we get the below equation.

$$n = n_0 + \frac{dn}{dT}\frac{\alpha r^2}{\kappa} I \tag{2.1.2.10}$$

Hence, the resulting nonlinear refractive index n_2 arising from the photo-thermo-optical effect is illustrated below.

$$n_2 = \frac{dn}{dT}\frac{\alpha r^2}{\kappa} \tag{2.1.2.11}$$

In the case of silicon, with the photo-thermo-optical effect, the nonlinear refractive index , denoted as n_2, is significantly enhanced to a value of $10^{-6}\ \mu m^2/mW$[19] which is three orders higher than the nonlinear refractive index caused by Kerr nonlinearity. With the refractive index change resulting from photo-thermo-optical nonlinearity, both sublinear and superlinear nonlinearity phenomena can be observed. **Fig. 2.1.4** is the scattering spectrum and absorption spectrum at different temperatures. We choose the same size in **Fig. 2.1.2** because of consistency**.** We can observe that both the scattering and absorption spectrum exhibit redshift as the temperature increases. According to our previous research[22], as the laser wavelength is shorter than the resonance wavelength (the black line 1 in the scattering spectrum of **Fig 2.1.4**), the scattering signal decreases as the temperature increase. As a result, we observe sublinear nonlinearity. Similarly, as the wavelength of laser exceeds the wavelength of the resonance(the black curve 2 in the scattering spectrum), the scattering signal increases as the temperature increase. Therefore, we observe superlinear nonlinearity.

In our previous research[22], we use a single-wavelength laser beam to induce the photo-thermo-optical nonlinearity and Mie resonance on a silicon nanoblock. Besides,

doi:10.6342/NTU202301642

the nonlinear refractive index n_2 reaches to 10^{-1} $\mu m^2/mW$ which is five orders greater than the nonlinear refractive index of bulk silicon.

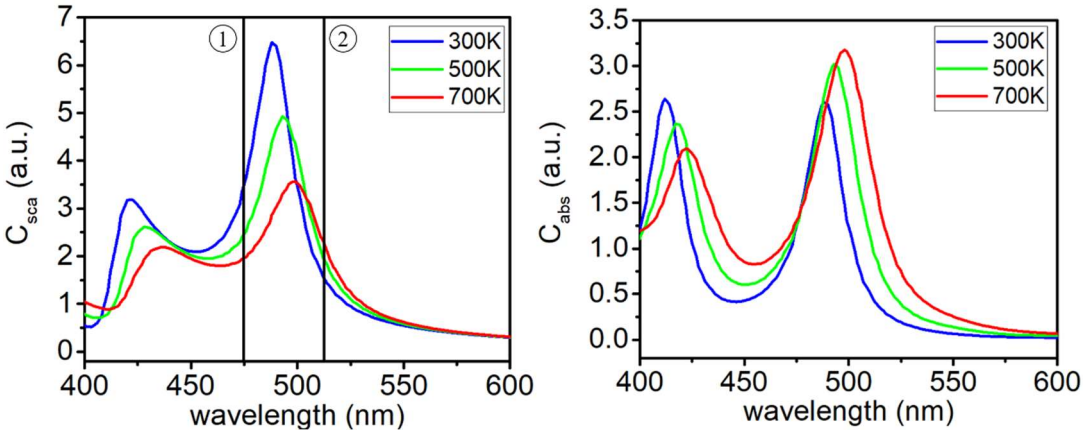

Figure 2.1.4: The spectrum of nanosphere at different temperatures.
(a)Scattering spectrum and (b) the spectral absorption properties of a 110 nm diameter silicon nanosphere. The black curves in the scattering spectrum represent two cases, one is the excitation wavelength on the left of the resonance peak, and the other is the excitation wavelength on the right of the resonance.

2.2 Optical Bistability

Optical bistability provides a large state transition in excitation intensity dependence which is suitable for many applications. The definition of optical bistability is that the output signal of an optical device is a multivalued function of the input intensity. With a small change in the input intensity, the temperature of the nanostructure will increase significantly causing the refractive index to change enormously[20]. As a result, the output signal will have large and sharp nonlinearity compared with photo-thermo-optical nonlinearity. The most typical example of an optical bistable device is a Fabry-Perot cavity. The medium inside is a nonlinear optical material with an intensity-dependent refractive index. The schematic of the Fabry-Perot cavity is presented in **Fig. 2.2.1** which is from a published paper [8]. The Fabry-Perot cavity consists of two identical mirrors with reflectivity R and a nonlinear medium with the nonlinear refractive index n_2. Assume that the incident intensity I_0 is a plane wave incident light and the output

doi:10.6342/NTU202301642

intensity I_t is the transmission signal. The relation between the input signal and output signal can be determined by the below equation[33].

$$I_t = \frac{1}{1 + F\sin^2(\delta/2)} I_0 \qquad (2.2.1)$$

Where $F = 4R/(1-R)^2$ and δ is the phase shift with respect to one round trip of the intracavity signal. The phase shift δ is shown below.

$$\delta = \frac{4\pi}{\lambda} L\cos\theta \cdot (n_0 + \Delta n) = \frac{4\pi}{\lambda} L\cos\theta \cdot (n_0 + n_2 I_i) \qquad (2.2.2)$$

Where λ represent the wavelength of the incoming plane wave, and let L denote the size of the cavity, θ is the incident angle, I_i denotes the total intensity of intracavity field which are the forward intracavity intensity I_i^+ and backward intracavity intensity I_i^- as presented in **Fig. 2.2.1,** n_2 denotes the nonlinear refractive index, n_0 denotes the linear refractive index.

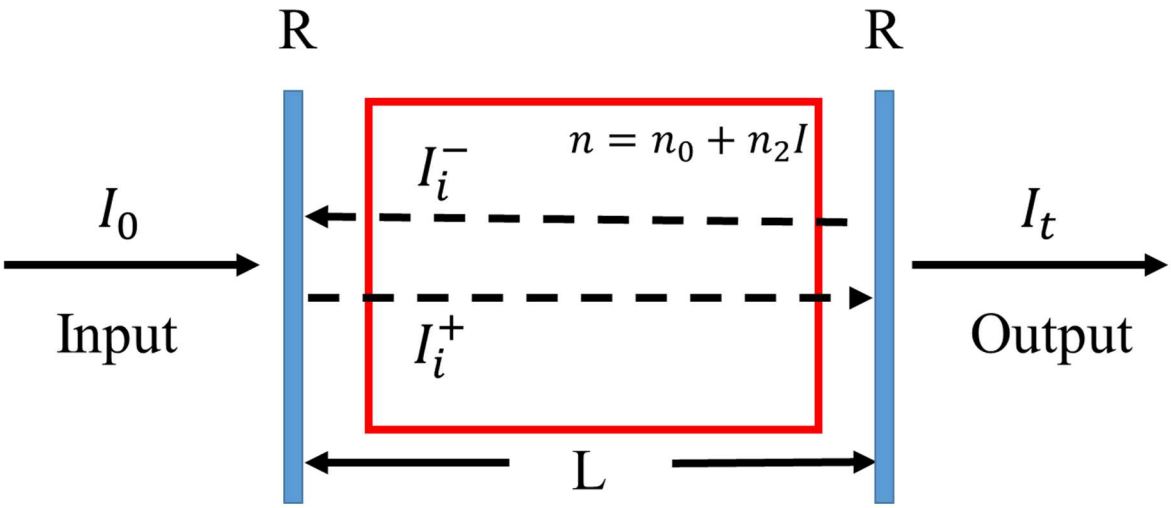

Figure 2.2.1 Structure of a nonlinear medium Fabry-Perot cavity

The relation of the intracavity intensity (I_i^+,I_i^-) and the incident intensity I_0 are shown below[8].

$$I_i^+ = \frac{1}{1-R} \cdot \frac{1}{1 + F\sin^2(\delta/2)} I_0 \qquad (2.2.3)$$

$$I_i^- = \frac{R}{1-R} \cdot \frac{1}{1 + F\sin^2(\delta/2)} I_0 \qquad (2.2.4)$$

doi:10.6342/NTU202301642

With **Eq. 2.2.3** and **Eq. 2.2.4**, the total intracavity intensity is shown below[8].

$$I_i = I_i^+ + I_i^- = \frac{1+R}{1-R} \cdot \frac{1}{1+F\sin^2(\delta/2)} I_0 = \frac{1+R}{1-R} I_t \quad (2.2.5)$$

We can replace **Eq.2.2.2** into **Eq.2.2.1** and rewrite **Eq. 2.2.5**.

$$\begin{cases} T = \dfrac{I_t}{I_0} = \dfrac{1}{1 + F\sin^2 \dfrac{1}{2}(\delta_0 + \gamma I_i)} \\ T = \dfrac{1+R}{1-R} \cdot \dfrac{1}{I_0} I_i \end{cases} \quad (2.2.6)$$

$$\begin{cases} \delta_0 = \dfrac{4\pi}{\lambda} n_0 L \cos\theta \\ \gamma = \dfrac{4\pi}{\lambda} n_2 L \cos\theta \end{cases} \quad (2.2.7)$$

The transmission signal T has to satisfy both equations in **Eq.2.2.6[8]**. Although we can numerically solve **Eq.2.2.6**, it is more straightforward to solve the equation graphically as **Fig. 2.2.2** shows. The first equation in **Eq. 2.2.6** is a periodic function with respect to $\delta_0 + \gamma I_i$. The second equation in **Eq. 2.2.6** is a linear function in which the slope is inversely related to the incident intensity I_0. Therefore, when the incident intensity increases, the slope is smoother as **Fig. 2.2.2 (A)** shows. The cross points between the periodic function and the linear function are the solution of the transmission signal. We can observe that there are two or three cross points at a certain incident intensity (range from I_1 to I_3) which indicates bistability.

With the bistability, the transmission signal of increasing incident intensity and decreasing incident intensity follow different routes as Fig. 2.2.2 (B) shows. When the incident intensity increases, the transmission signal follows the lower branch from A to C. At the state transition incident intensity I_3, the transmission signal suddenly increases to D. When the incident intensity decreases, the transmission signal follows the upper branch from E to G and suddenly decreases to A at the state transition incident intensity I_1. As a result, the output signal follows different routes when we increase and decrease

doi:10.6342/NTU202301642

the incident intensity. This phenomenon is called the hysteresis effect. We can observe that the range of the hysteresis effect is from I_1 to I_3 which is also the range of bistability from Fig. 2.2.2 (A) Therefore, the hysteresis effect comes from bistability. Besides, there is a study[4] theoretically proving that the slope at the state transition incident intensity approaches infinity. As a result, the transmission signal will have an ultra-large and sharp change at the state transition incident intensity (I_1, I_3) as **Fig. 2.2.2 (B)** shows. With the ultra-large and sharp change in optical bistability, there are many applications, such as all-optical switching[34].

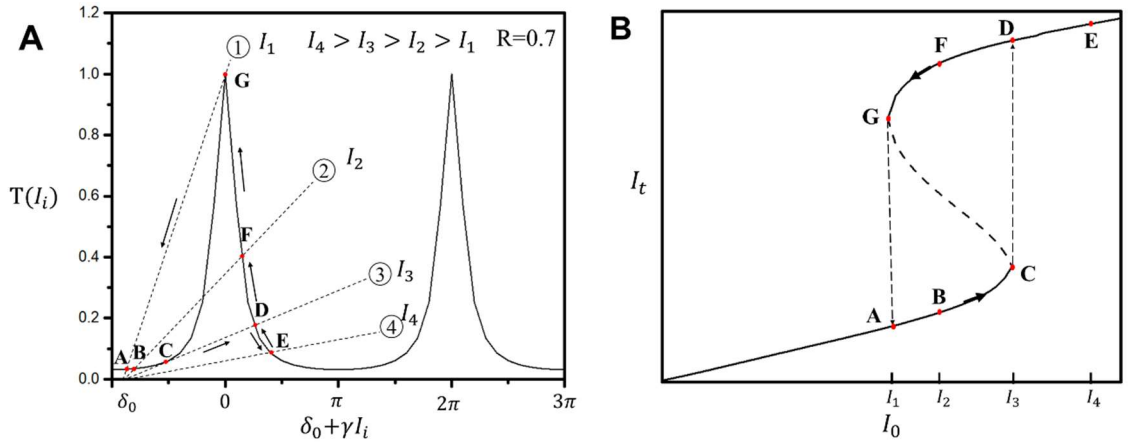

Figure 2.2.2 Schematic of optical bistability

(A) is the graphical solution of the transmission signal with different incident intensities. The refractive index of both mirrors is 0.7. The label 1 to 4 correspond to four different incident intensities where $I_4 > I_3 > I_2 > I_1$. The labels A to G correspond to the intersection points of different incident intensities.

(B) is the hysteresis behavior of the Fabry-Perot cavity [8]. I_0 represents the incident intensity and I_t is the intensity of the transmission signal. The labels A to G correspond to the intersection points of different incident intensities.

From the above discussion, we know that optical bistability requires a resonator and a nonlinear medium. In a recent study[20], they use a micrometer scale cylinder to form a Mie resonator and use a laser source to induce photo-thermo-optical nonlinearity. Since optical bistability is induced by the photothermal effect, we called it photothermal bistability. With photothermal bistability, they devise an optimized design aimed at achieving efficient nonlinear optical heating. Typically these kinds of structures require

doi:10.6342/NTU202301642

micrometer scale high Q factor structure to compensate for the low nonlinear refractive index ($n_2 \sim 10^{-6}\ \mu m^2/mW$). Our recent research has released this requirement in a silicon nanoblock with Q factor around 10, by combining the photothermal effect and Mie resonance to achieve high nonlinear refractive index ($n_2 \sim 10^{-1}\ \mu m^2/mW$) [22]. Therefore, it is worth exploring photothermal bistability in a single silicon nanoblock.

In this study, we use the simulation model in **Section 3.2** to predict which sizes of nanoblock have photothermal bistability. We use laser scanning microscopy with a 561 nm CW laser to observe photothermal bistability in a single nanoblock. The setup is shown in **Section 3.2**. The results of the observation of photothermal bistability from a single silicon nanoblock and other properties of photothermal bistability are shown in **Chapter 4**.

doi:10.6342/NTU202301642

Chapter 3 Method

This chapter explains details regarding the experiment and numerical simulation, including the simulation setup, the principle of laser heating simulation, the optical setup of laser scanning microscopy, and the sample description.

3.1 Finite Element Method

From **Section 2.1.1**, the analytical solution is only available for sphere structure. To study the optical properties of silicon nanoblock, we use the finite element method (FEM) by RF module in COMSOL *Multiphysics* (COMSOL, Inc.). In a linear homogeneous isotropic medium with permittivity ϵ and permeability μ, Maxwell's equations are given as the vector Helmholtz equations as shown below[35].

$$(\nabla^2 - \mathrm{k}^2)\vec{\mathrm{E}}(\vec{\mathrm{r}}) = 0 \qquad (3.1.1)$$

Where $\vec{\mathrm{E}}(\vec{\mathrm{r}})$ denotes the electric field, $\vec{\mathrm{r}}(x, y, z)$ denotes the position, and $k^2 = \epsilon\mu\omega^2$ is the wavenumber vector with angular frequency ω. The principle of FEM is to solve the weak formulation of **Eq. 3.1.1**. The weak formulation is multiplied by a test function ϕ on **Eq. 3.1.1** and integrated over the domain Ω. The formulation is shown below.

$$\int_{\Omega} [(\nabla^2 - \mathrm{k}^2)\mathrm{E}(\vec{\mathrm{r}})]\phi(\vec{\mathrm{r}})\mathrm{dV} = 0 \qquad (3.1.2)$$

We consider the test function ϕ and the solution E as elements of Hilbert spaces. The weak formulation is obtained by enforcing the equality given by **Eq. 3.1.1** to be satisfied for all test functions within the Hilbert space. The reason to call it "weak" is that it relaxes the requirement **Eq. 3.1.1**, which requires equality to hold for all points in the calculation domain. **Eq. 3.1.3** only requires equality to hold in an integral sense. Given that both the test function ϕ and the solution E reside within a Hilbert space, we can represent the solution E as a linear combination of a set of basis functions ϕ belonging to the subspace:

doi:10.6342/NTU202301642

$$E(\vec{r}) = \Sigma_i E_i \phi_i(\vec{r}) \quad (3.1.3)$$

Below is the discretized form of **Eq. 3.1.2** for each test function $\phi_i(\vec{r})$.

$$\Sigma_i E_i [(\nabla^2 - k^2)\phi_i(\vec{r})]\phi_j(\vec{r})dV = 0 \quad (3.1.4)$$

The dimensionality of **Eq. 3.1.4** aligns with that of the finite-dimensional function space. Considering the utilization of n test functions ϕ_j, where j ranges from 1 to n, we can establish n equations based on **Eq. 3.1.4**, involving n unknown coefficients E_i. By incorporating the discretized system and boundary condition, we can solve a system of linear equations.

$$A\vec{E} = 0 \quad (3.1.5)$$

Where $\vec{E}$ is the vector of unknowns, $\vec{E} = \{E_1, \dots, E_I, \dots, E_n\}$, and A is an $n \times n$ matrix that encompasses the coefficients of E_i in each equation j, with its elements denoted as A_{ji}. To solve this linear equation, we can use either an iterative solver based on the conjugate gradient method[36] or a direct solver based on LU decomposition[37]. The accuracy of the simulation result depends on the mesh size. When the mesh size becomes smaller, the calculation time increases. The details of the simulation setting including the mesh size and some physics settings are discussed in **Section 3.2.**

3.2 Laser Heating Simulation

In **Section 2.1.2**, we describe that the photo-thermo-optical effect contains two processes: the photothermal effect and the thermo-optical effect. To simulate this, we need the radio frequency module (RF) and the heat transfer module (HT) in COMSOL *Multiphysics* (COMSOL, Inc.). In this study, we use two methods to do the simulation, which are separate model and combination model

In the separate model, we simulate the RF module and HT module separately and use iterative ways to calculate the equilibrium temperature. The advantage of this method

doi:10.6342/NTU202301642

is that it can solve the equilibrium temperature in a graphical way similar to **Fig. 2.2.2.** Therefore, we can determine whether there is bistability directly. However, because this method simulates the photo-thermo-optical effect separately, only the cross points are the actual physical solution. Therefore, it can't simulate how temperature evolves with time. Besides, this method is time-consuming and takes three days to calculate an excitation intensity dependence of one size of the nanostructure.

In the combination model, we combine the RF and HT modules to get the equilibrium temperature directly. Since this method can simulate the photo-thermo-optical effect simultaneously, it can calculate how temperature evolves with time and laser scanning simulation. Therefore, in **Section 4.3**, we use this method to do the temporal simulation. Also, it takes only 6 hours to calculate an excitation intensity dependence of one size of the nanostructure. In this study, we mainly use this method to quickly simulate each size of the nanoblock.

The details of the simulation setting are shown in **Fig. 3.2.1** and **Table 3.2.1.** The computational region is a spherical domain with a radius of 1200 nm, where the upper hemisphere is quartz substrate and the lower hemisphere is oil. The silicon nanoblock is on the quartz immersed in oil sitting in the center of the calculation domain. To calculate the backward scattering, we set a monitor surface in front of the boundary of the calculation domain, where the area is determined by the numerical aperture of the objectives. The scattering cross-section is determined by the integration of time-averaged scattering intensity on the monitor surface divided by the intensity of the light source. The equation is shown below.

$$C_{sca} = \frac{\int_S \vec{S}_{sca} \cdot d\vec{A}}{|\vec{S}_{inc}|} \qquad (3.2.1)$$

Where S in the subscript of the integration denotes the monitor surface. Since we want

doi:10.6342/NTU202301642

to simulate the photo-thermo-optical effect, we need the refractive index of silicon with temperature variation. The refractive index is measured by ellipsometry[22], and we use the following equation[38] to extend the complex refractive index up to 1500K. The temperature-dependent refractive index is shown in **Fig. 3.2.2.**

$$n(T) = a_n(T - 300) + n_n \quad (3.2.2)$$

$$k(T) = a_k \exp(\frac{T}{T_k}) \quad (3.2.3)$$

Where n(T) denotes the real component and k(T) denotes the imaginary component, and a_n, n_n, a_k, T_k are $2.88 \times 10^{-4}, 3.98, 1.04 \times 10^{-2}, 353[K]$, respectively.

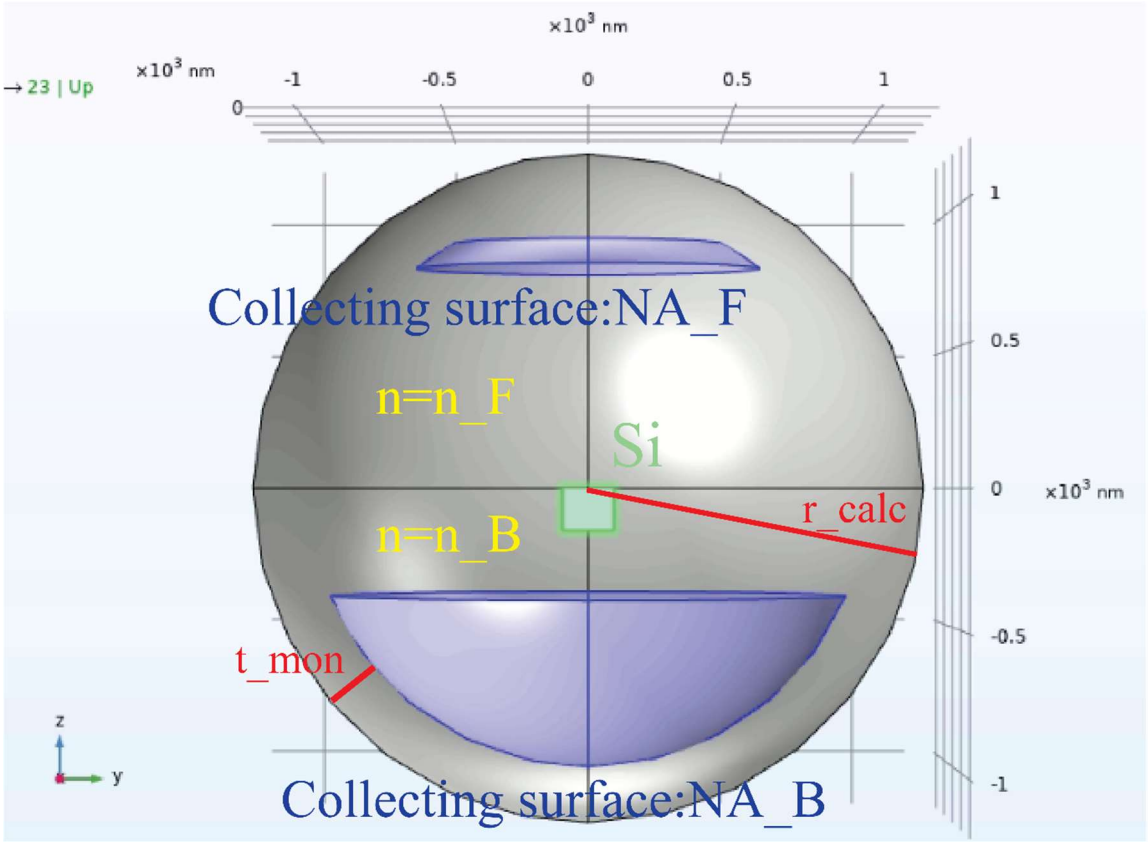

Figure 3.2.1: Schematic of the simulation setup.

The green square in the center is the location of our silicon nanoblock and the center is located at z=$\frac{-15}{2}$ nm. The notations r_calc and t_mon indicate the radius of the calculation domain and the distance between the monitor surface and the calculation domain. The two blue surfaces are the monitor surfaces corresponding to the NA for collection in forward (+z) and backward (-z) regions, respectively. The medium in +z is defined with a refractive index n_F, and the medium in -z is defined with a refractive index n_B. The detailed parameters are listed in **Table 3.2.1.**

doi:10.6342/NTU202301642

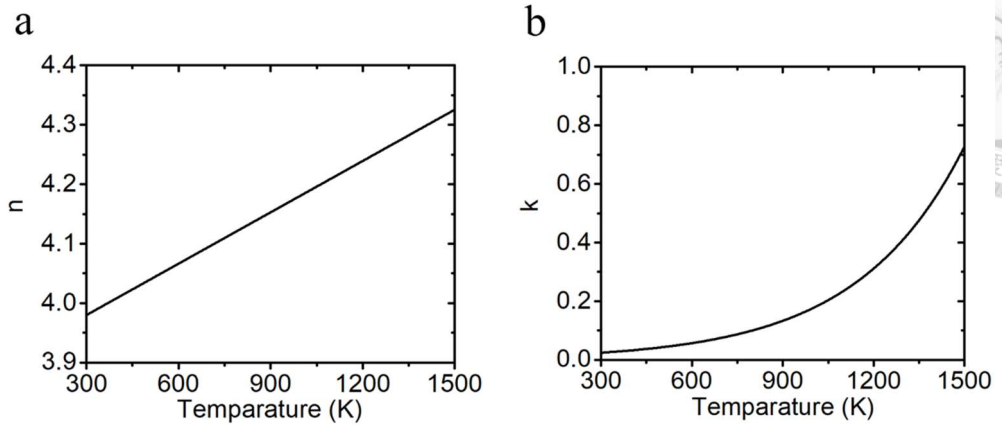

Figure 3.2.2 Refractive index of crystal silicon with temperature variation at 561 nm[22]
(a) presents the real component and (b) presents the imaginary component.

Table 3.2.1: Parameters used in the simulation.

Name	Description	Value
n_F	The refractive index of materials in $z > 0$ regions.	1.46
n_B	The refractive index of materials in $z < 0$ regions.	1.518
r_calc	The radius of the calculation domain.	1200 nm
t_mon	The numerical	200 nm
NA_B	The numerical aperture of the objective lens.	1.4
w0	The full width at half maximum of the Gaussian beam intensity profile at the focal plane.	$\frac{0.51\lambda}{NA} = 204.44$ nm

In the RF module, we use scattering boundary conditions (SBC) to avoid the back reflection of the outgoing wave. The light source we used is a tightly focused Gaussian electromagnetic wave with a wavelength of 561 nm and the corresponding full-width half maximum is shown in **Table 3.2.1.** The Gaussian wave is impinged towards the quartz side, originating from the oil side. In the HT module, we use the convective heat flux boundary condition to model general heat losses. The formulation of the HT module is shown below.

$$\rho C_p \frac{\partial T}{\partial t} - \kappa \nabla^2 T = Q \qquad (3.2.4)$$

Where Q denotes the heat source, κ denotes the thermal conductivity, C_p denotes the heat capacity, and ρ indicates the material density, the corresponding values are shown in **Table 3.2.2.**

doi:10.6342/NTU202301642

Table 3.2.2: The material properties for the thermal simulation.

Material	$\rho(kg \cdot m^{-3})$	$C_p(J \cdot kg^{-1} \cdot K^{-1})$	$\kappa(W \cdot m^{-1} \cdot K^{-1})$ (as a function of T)
Silicon	2329	712	160-20
Quartz	2648	739	11.52-1.29
Oil	1050	1000-1240	0.14-0.016

3.2.1 Separate Model

In the separate model, we simulate the RF module and HT module separately. First, we use the RF module to simulate the absorption cross-section as **Figure 3.2.3** red curve shows. Then, we set the heat source Q as the below equation and simulate the equilibrium temperature with different laser intensities and absorption cross-sections as **Figure 3.2.3** blue and green curves show.

$$Q = \frac{F \cdot C_{abs}}{V} \qquad (3.2.1.1)$$

Where V is the volume of the silicon nanoblock, F is the laser heat flux as shown below, and $C_{abs}$is the absorption cross-section.

$$F = \frac{2P_{in}}{\pi w_b^2} \exp\left(\frac{-2((x-x_0)^2 + (y-y_0)^2)}{w_b^2}\right) \qquad (3.2.1.2)$$

Where P_{in} denotes the laser power, w_b denotes a beam radius. The center position of the beam is denoted by x0 and y0. From **Fig. 3.2.3 (A),** we can regard the red curve as the heat source term (Q) in **Eq. 3.2.4** and the blue and green curves as the heat dissipation term ($\kappa\nabla^2 T$) in **Eq. 3.2.4.** Therefore, the equilibrium temperature occurs when the heat source equal to the heat dissipation which is the cross point in **Fig. 3.2.3 (A).** With the equilibrium temperatures, we use the temperature-dependent backward scattering cross-section from **Fig. 3.2.3 (B)** to get the corresponding scattering cross-section**.** The comparison of the experiment results and simulation results is shown in **Fig. 3.2.4.** We observe that the simulation matches well with the experiment. In **Fig. 3.2.4**, circle 1 and circle 2 are the scattering intensity corresponding to the laser intensity 10 $mW/\mu m^2$ and 20 $mW/\mu m^2$ in **Fig. 3.2.3 (A)**.

doi:10.6342/NTU202301642

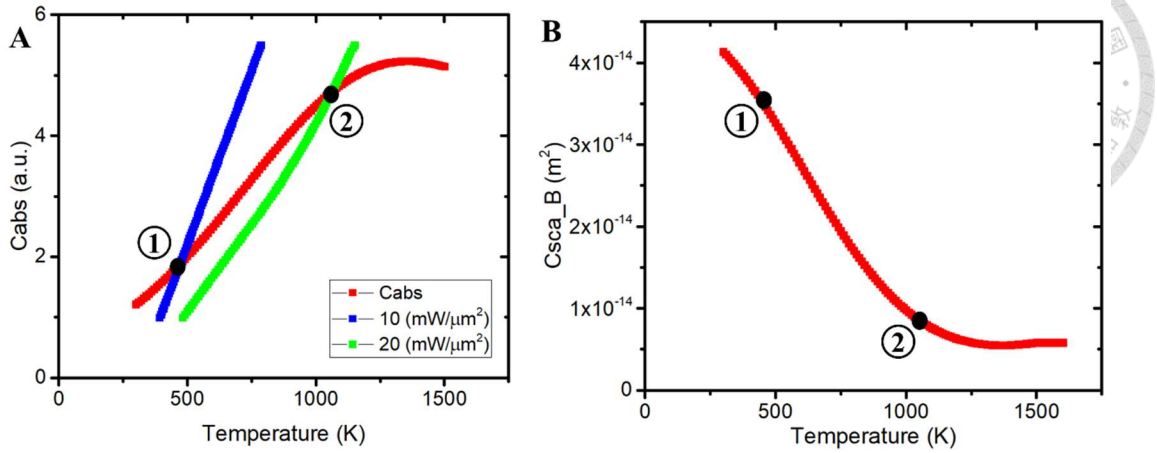

Figure 3.2.3 Schematic of the separate model

The figures are examples of a 180 nm-wide silicon nanoblock with a height of 150 nm. In **Figure (A)**, the red curve is the absorption cross-section with temperature variation calculated by the RF module. The blue and green curves are the temperature calculated by the HT module with different absorption cross-sections and certain laser intensities. The laser intensity of blue and green are 10 $mW/\mu m^2$ and 20 $mW/\mu m^2$ respectively. Circle 1 and circle 2 are the cross points corresponding to the laser intensity 10 $mW/\mu m^2$ and 20 $mW/\mu m^2$ respectively. In **Figure (B)**, the red curve is the temperature-dependent backward scattering cross-section calculated by the RF module. Circle 1 and circle 2 are the cross points corresponding to the laser intensity 10 $mW/\mu m^2$ and 20 $mW/\mu m^2$ respectively.

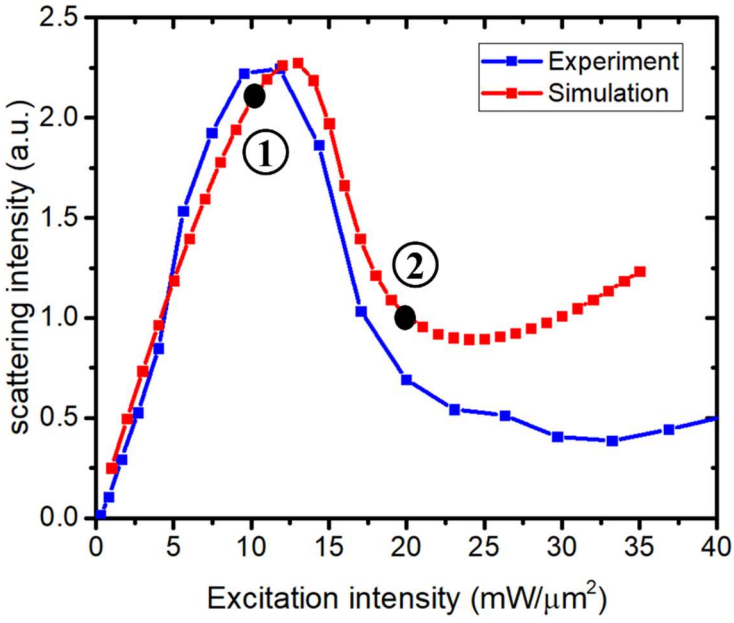

Figure 3.2.4: Comparison of experiment result and simulation result of the separate model.

The figure is an example of a 180 nm-wise silicon nanoblock with a height of 150 nm. The blue curve is the result of the experiment which is from our recent publication[39]. The red curve is the simulation result of the separate model. Circle 1 and circle 2 are the scattering intensity corresponding to the laser intensity 10 $mW/\mu m^2$ and 20 $mW/\mu m^2$ from **Fig. 3.2.3 (A).**

doi:10.6342/NTU202301642

3.2.2 Combination Model

In the combination model, we use the Multiphysics module to combine the RF module and HT module. We don't need to set the heat source, because the model calculates itself through the below equation.

$$Q = Q_{rh} + Q_{ml} \tag{3.2.2.1}$$

$$Q_{rh} = \frac{1}{2} Re(\boldsymbol{J} \cdot \boldsymbol{E}) \tag{3.2.2.2}$$

$$Q_{ml} = \frac{1}{2} Re(i\omega \boldsymbol{B} \cdot \boldsymbol{H}) \tag{3.2.2.3}$$

Where E denotes the electric field intensity, H denotes the magnetic field intensity, and B denotes the density of magnetic flux, Q_{rh} is the resistive loss, Q_{ml} is the magnetic loss, J denotes the current density. In this method, the model does the iteration of the laser heating process itself and gets the equilibrium directly. The comparison of the experimental results and simulation results are presented in **Fig. 3.2.5.** The simulation result matches well with the experiment result.

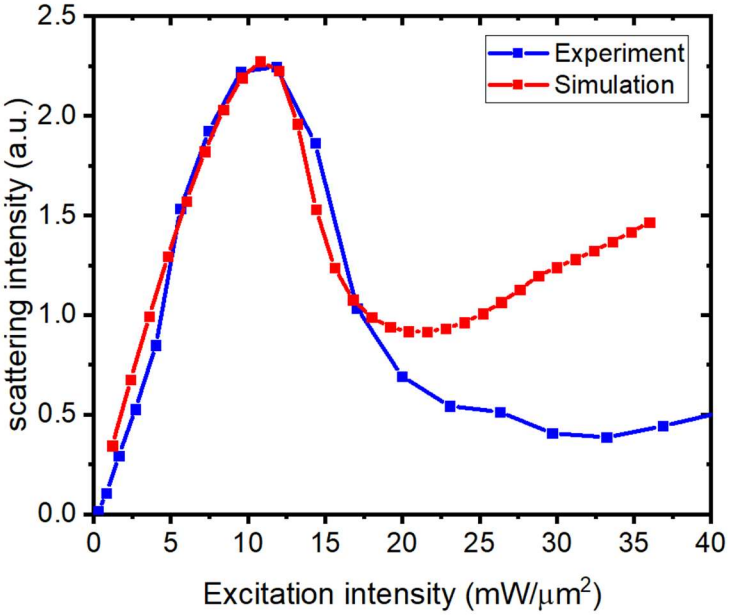

Figure 3.2.5: Comparison of experiment result and simulation result of combination model.
The figure is an example of a 180nm-wide silicon nanoblock with a height of 150 nm. The blue curve is the result of the experiment which is from our recent publication[39]. The red curve is the simulation result of the combination model.

doi:10.6342/NTU202301642

3.3 Laser Scanning Microscopy

For this study, scanning images of the silicon nanoblock were acquired by integrating a commercial laser scanning system (FV-300, Olympus, Japan) with an inverted microscope (IX-71, Olympus, Japan). The scanning plane is on the X-Y plane of the sample as **Fig. 3.3.1** shows. The illumination employed in the experiment is provided by a continuous-wave laser emitting at a wavelength of 561 nm with a power of 150 mW. To regulate the intensity of the light source, the light is directed through an attenuator consisting of a polarization beam splitter and a half-wave plate. Subsequently, the light source is introduced into the laser scanning system. The scanning process is conducted by a pair of galvo mirrors at a rate of 3 μs per pixel. The light is directed precisely towards the sample using a high-NA objective lens (UPlanSApo ×100 oil, NA=1.4, Olympus, Japan). The second half-wave plate under the objective lens is treated as a polarizer to make sure the light source impinging on the sample is linearly polarized in the x direction of the scanning image. The backward scattering signals go back through the same path and are extracted with a 50/50 beam splitter. After reflecting by a mirror and passing through a confocal pinhole, the signals are collected by a built-in backward photomultiplier tube (PMT). The pinhole in front of the pinhole is used to eliminate the out-of-focus signal.

doi:10.6342/NTU202301642

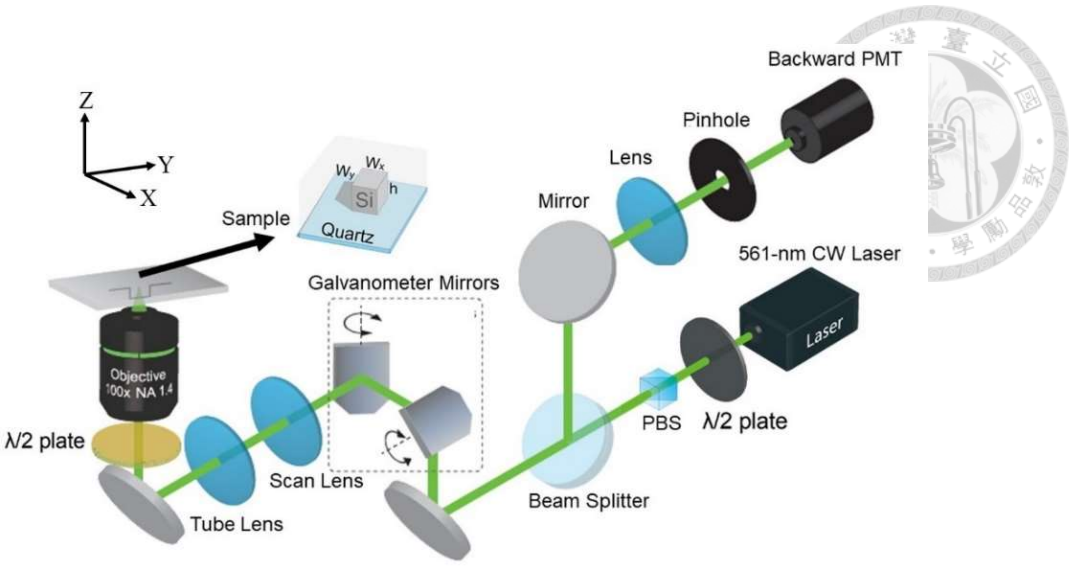

Figure 3.3.1: Schematic of laser scanning microscope setup.
The sample was facing downward**.** The graph is reproduced from [40].

3.4 Sample Fabrication

The focus of this study is on monocrystalline silicon nanoblocks. These nanoblocks have a consistent height of 150 nm, while their widths $(w_x = w_y = w)$ vary from 80 nm to 280 nm in increments of 10 nm. The sample is on a quartz substrate submerged in index-matching oil (refractive index n=1.518). The fabrication process composes of four steps. First, the monocrystalline silicon with 150 nm thickness is bonded to the surface of a quartz substrate using wafer bonding technique.[41]. Next, a chemical resilience was applied to the silicon wafer using spin coating, followed by the creation of nanostructure patterns through electron beam lithography. Third, a Cr mask pattern was formed by evaporating a Cr layer on the sample and lifting off the resist. Fourth, the nanoblock nanostructure was made by etching the Si layer with plasma gases and removing the Cr mask. These nanoblocks are provided by our collaborators from Osaka University[42].

doi:10.6342/NTU202301642

Chapter 4 Results

In this chapter, we use the verified simulation to predict which sizes of nanostructure have photothermal bistability and show the properties of photothermal bistability: the hysteresis effect and transient effect. We also show the generality of the size and wavelength dependency of photothermal bistability. In the end, we show the experiment result and compare it with the simulation result to verify the correctness of the simulation.

4.1 Prediction of Photothermal Bistability with Intensity Dependent Scattering

In **Section 2.2**, we want to observe photothermal bistability in crystal silicon nanoblock. To predict which sizes of nanoblock have photothermal bistability, we use the combination model in **Section 3.2.2** and the parameters setting in **Table 3.2.1** to quickly simulate each size of the nanoblock. We find that when silicon nanoblock with widths of 110-150 nm, there is a large state transition in excitation intensity dependence which cannot be explained by our previous study[22]. When the size is 80-100 nm and 160-280 nm, there is a smooth variation in excitation intensity dependence which can be explained by our previous study. Therefore, to compare the difference between these two types of nonlinearity, we show the result of w=110 nm and w=180 nm nanoblock. The results are presented in **Figure 4.1.1**. In **Figure 4.1.1(b),** we can observe a sublinear nonlinearity. However, in **Figure 4.1.1 (a)**, there is an ultra-large and sharp nonlinearity when the intensity is at 19.0 $mW/\mu m^2$.

doi:10.6342/NTU202301642

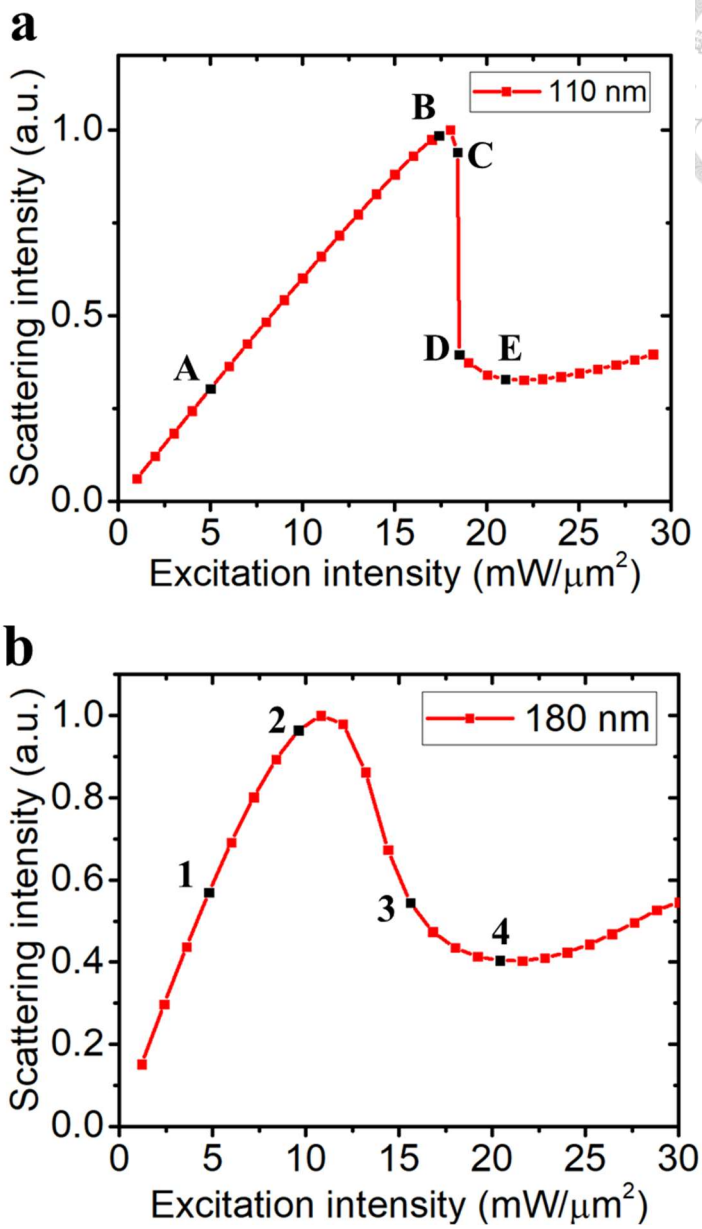

Figure 4.1.1 Simulation results of intensity dependency scattering from combination model
Where (a) and (b) are the results of silicon nanoblock with widths of 110 nm and 180 nm respectively. The denotations A~E correspond to the cross points from separate model in **Fig. 4.1.2 (a).** The denotations 1~4 correspond to the cross points from separate model in **Fig. 4.1.2 (b).**

To check whether there is photothermal bistability, we use the separate model in **Section 3.2.1** to see whether there are multiple cross points**.** The simulation results of silicon nanoblock with widths of 110 nm and 180 nm are presented in **Fig. 4.1.2(a)** and **(b)**. The black curve represents the heat source and the blue, green, orange, and red curves represent the heat dissipation with different excitation intensities. The cross points in **Fig.**

doi:10.6342/NTU202301642

4.1.2 are the solutions of equilibrium temperatures as mentioned in **Section 3.2.1.** In **Fig 4.1.2 (b),** there is one cross point for each intensity. As a result, there is one equilibrium temperature for each intensity. In **Fig. 4.1.2 (a),** we can observe that there are two cross points when the intensities are between 17.4 $mW/\mu m^2$ and 18.4 $mW/\mu m^2$. This means that two possible equilibrium temperatures indicate the phenomenon of bistability. When the intensity is at 18.4 $mW/\mu m^2$, the heat source (black curve) is above the heat dissipation (orange curve) before cross point C. Therefore, from **Eq. 3.2.4**, the temperature increases from room temperature to cross point C (around 750 K). After cross point C, the heat source is still above heat dissipation. The temperature increases to cross point D (around 1400 K). After cross point D, the heat source is below heat dissipation causing the temperature to decrease. As a result, the temperature increases from around 750 K (cross point C) to around 1400 K (cross point D) causing the output signal to change significantly.

As mentioned in **Section 2.2**, at the state transition excitation intensity, the equilibrium state suddenly jumps from one state to another state causing a very sharp change in the output signal. Since the bistability is induced by the photothermal effect, we name the mechanism photothermal bistability. With the bistability, we should also observe the hysteresis effect mentioned in **Section 2.2.** The details of the hysteresis effect are shown in **Section 4.2.**

doi:10.6342/NTU202301642

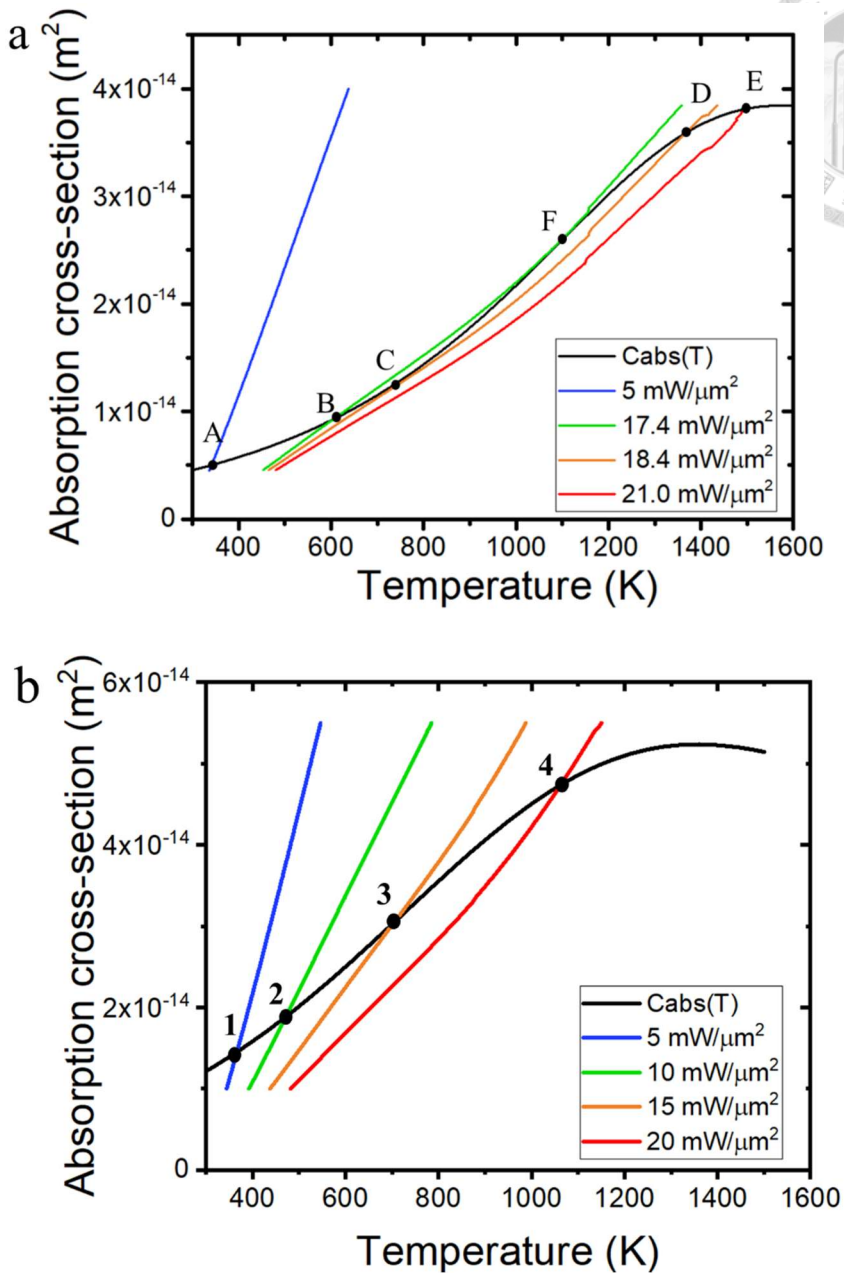

Figure 4.1.2 Simulation results of intensity dependency scattering from separate model

(a) is the result of a 110 nm-wide silicon nanoblock. The black curve represents the absorption cross-section with temperature variation. The blue, green, orange, and red are the heat dissipation at different excitation intensities corresponding to 5 $mW/\mu m^2$, 17.4 $mW/\mu m^2$, 18.4 $mW/\mu m^2$, and 21.0 $mW/\mu m^2$ respectively. The denotations A~F correspond to the cross points of the four excitation intensities. (b) is the result of a 180 nm-wide silicon nanoblock. The black curve represents the absorption cross-section with temperature variation. The blue, green, orange, and red are the heat dissipation at different excitation intensities corresponding to 5 $mW/\mu m^2$, 10 $mW/\mu m^2$, 15 $mW/\mu m^2$, and 20 $mW/\mu m^2$ respectively. The denotations 1~4 correspond to the cross points of the four excitation intensities.

doi:10.6342/NTU202301642

4.2 Hysteresis Effect of Photothermal Bistability

We have proved that the ultra-large and sharp nonlinearity comes from the photothermal bistability in **Section 4.1**. Besides, we show that with the bistability, there is a hysteresis effect in **Section 2.2.** In this section, we utilize the combination model in **Section 3.2.2** to show the hysteresis effect of the photothermal bistability of a 110 nm-wide silicon nanoblock. The result is presented in **Fig. 4.2.1.** The hysteresis effect contains two parts: increase excitation intensity (red curve in **Fig. 4.2.1**) and decrease excitation intensity (blue curve in **Fig. 4.2.1**). We simulated the equilibrium temperature of one excitation intensity and set it as the initial condition for the next excitation intensity. For example, when we increase the excitation intensity, we simulated the equilibrium temperature at 1 $mW/\mu m^2$ and set it as the initial temperature when the intensity increased to 2 $mW/\mu m^2$. With fine-tuning the excitation intensity, the range of the hysteresis loop is range from 17.4 $mW/\mu m^2$ to 18.4$mW/\mu m^2$. We can recall that in **Section 4.1**, the range of bistability is also from 17.4 $mW/\mu m^2$ to 18.4 $mW/\mu m^2$ in **Fig. 4.1.2(a).** Therefore, we can prove again that the hysteresis effect comes from bistability.

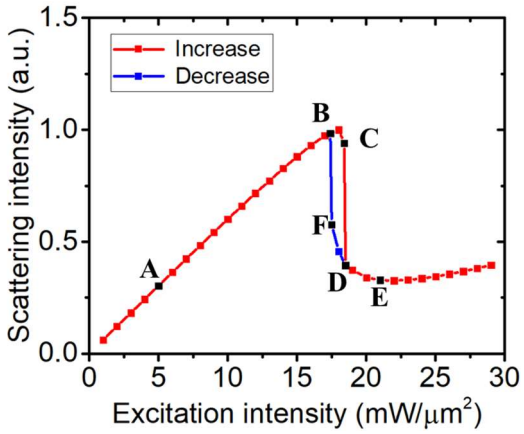

Figure 4.2.1 Hysteresis effect of photothermal bistability of nanoblock with a width of 110 nm
The graph is simulated from the combination model. The red curve is the result of increasing excitation intensity and the blue curve is the result of decreasing excitation intensity. The denotations A~F correspond to the cross points from separate model in **Fig. 4.1.2 (a).**

doi:10.6342/NTU202301642

4.3 Temporal Simulation of Photothermal Bistability

From **Section 4.2**, we know that at the state transition excitation intensity which is 18.4 $mW/\mu m^2$ from **Fig. 4.1.2(a),** the equilibrium temperature jumps from one state to another state causing the temperature to increase significantly. To understand how the temperature increase, we simulate the temporal evolution of the temperature of the 110 nm-wide silicon nanoblock at 18.4 $mW/\mu m^2$. We use the combination model in **Section 3.2.2** and do the frequency-transient study in COMSOL. In **Fig. 4.3.1**, we observe that the equilibrium time is around 10 μs which is four orders of magnitude higher than our previous study[22]. Besides, the process shows a two-step temperature increase. We can calculate the quantity of the time-dependent temperature ($\frac{\partial T}{\partial t}$) by subtracting the heat source with heat dissipation from **Eq. 3.2.4.** In **Fig 4.3.2(a)**, in the beginning, the heat source minus heat dissipation is large, causing the temperature to increase quickly. When the temperature is around 700 K, the heat source minus heat dissipation is nearly zero. Therefore, the temperature increases slowly around 700 K. When the temperature is around 1000 K, we can observe that there is a small increase of the heat source minus heat dissipation causing the temperature to increase quickly and finally stop at 1325 K.

We can compare the result from the combination model with the result from the separate model. In **Fig. 4.3.2(b)**, we can see that the heat source (blue curve) is close to heat dissipation (red curve) around cross point one. Therefore the temperature increases slowly around cross point one. After cross point one, the heat source becomes large causing the temperature to increase quickly to cross point two. After cross point two, the heat source minus heat dissipation is negative. As a result, the temperature tends to decrease back to cross point two. The temporal evolution of the temperature of the two simulation results matches well with each other. As we mentioned in **Section 3.2.1**, the

doi:10.6342/NTU202301642

heat source is proportional to the absorption cross-section from **Eq. 3.2.1.1**. With the temperature-dependent absorption cross-section, the temporal evolution of the temperature shows a micro-second scale two-step temperature increase. Besides, from a previous study[43], they experimentally show that the equilibrium time of their optical bistability nanostructure is around 5 μs. This can prove the validity of the micro-second scale two-step temperature increase.

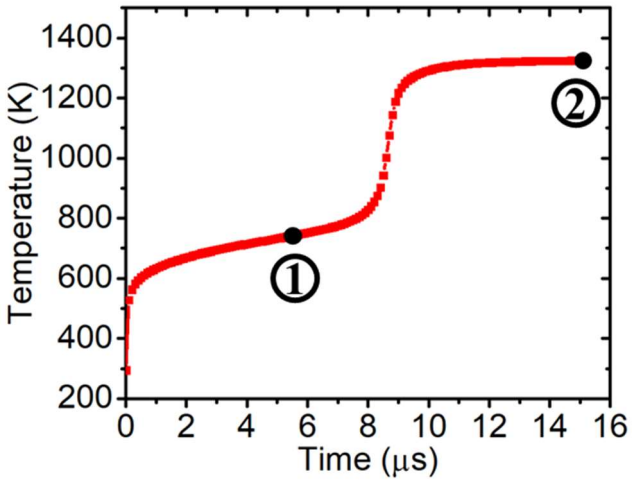

Figure 4.3.1 The temperature evolution of the 110 nm-wide silicon nanoblock over time.
The excitation intensity is fixed at 18.4 $mW/\mu m^2$. The circles represent the cross points in **Fig.4.3.2**.

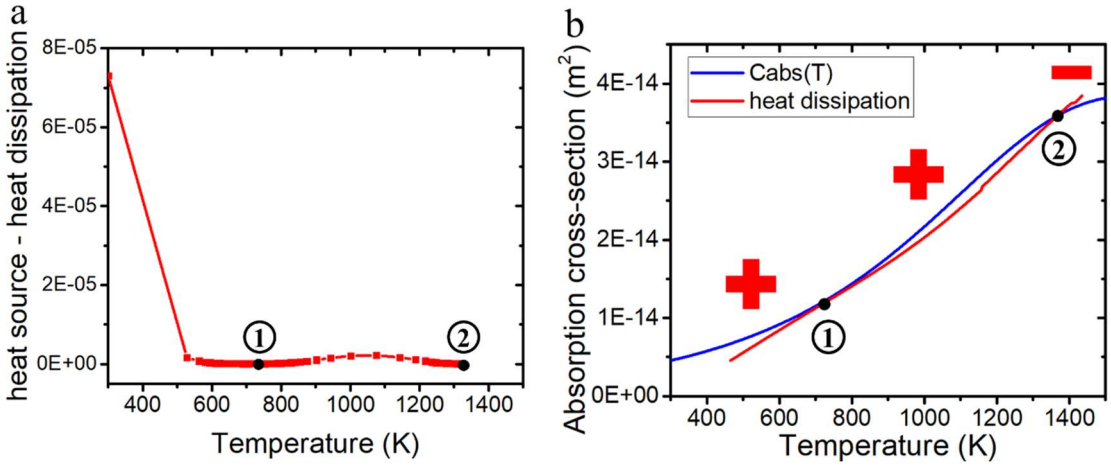

Figure 4.3.2 Heat source and heat dissipation at different temperatures.
The excitation intensity is fixed at 18.4 $mW/\mu m^2$. (a) is calculated from the combination model. (b) is calculated from the separate model. The blue curve is the absorption cross section which can be regarded as the heat source. The red curve is the heat dissipation. The circles represent the cross points one and two. The positive and negative signs indicate the sign of the heat source minus the heat dissipation.

doi:10.6342/NTU202301642

4.4 Size-Dependent and Wavelength-Dependent Photothermal Bistability

In **Section 4.1**, we mention that the nanoblocks with widths of 80 nm and 110-160 nm have a large transition in excitation intensity dependence. In this section, we present the simulation results of 110-150nm. From **Fig. 4.4.1**, we observe that the four sizes of the nanoblocks all show ultra-large and sharp nonlinearity. The threshold of the nonlinearity of w= 110 nm, 120 nm, 130 nm, 140 nm, and 150 nm are 18.4 $mW/\mu m^2$, 22 $mW/\mu m^2$, 23 $mW/\mu m^2$, 23 $mW/\mu m^2$, and 21 $mW/\mu m^2$ respectively. We can see that the threshold of the nonlinearity increases when the size increases from 110 nm to 140nm and decreases when the size increases from 140 nm to 150 nm. Therefore, by changing the size of the nanoblock, we can design the desired threshold of the photothermal bistability structures.

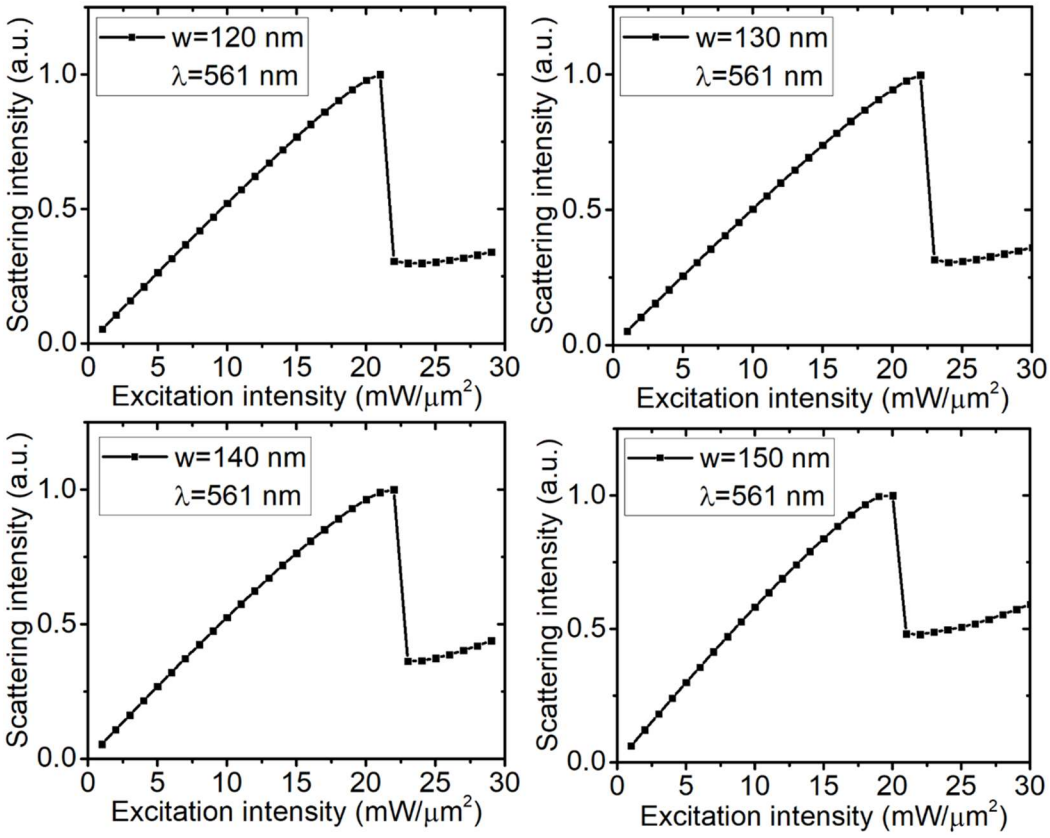

Figure 4.4.1 The intensity-dependent graph of nanoblock with widths of 120 nm-150 nm.

doi:10.6342/NTU202301642

Besides changing the size of the nanoblock, there are some studies [20, 44] showing that by detuning the distance of the laser wavelength and the resonance wavelength from the absorption spectrum, we can induce photothermal bistability. In **Section 4.1,** we compare the simulation result of nanoblock with widths of 110 nm and 180 nm and show that under a 561nm laser, there isn't photothermal bistability in nanoblock with a width of 180 nm. Therefore, we use the combination model in **Section 3.2.2** and try to induce photothermal bistability in w=180 nm nanoblock. In **Fig. 4.4.2**, we detune the distance of the laser wavelength and the resonance wavelength and eventually induce the photothermal bistability in w=180 nm nanoblock. **Fig. 4.4.2(a)** is the absorption cross-section spectrum of w=180 nm nanoblock. The resonance peak is at around 550 nm. After detuning the distance between the resonance peak and the laser wavelength, we induce photothermal bistability when the laser wavelength is at 644 nm. From **Fig. 4.4.2(b)**, we also observe sharp and strong nonlinearity similar to **Fig. 4.1.1(a).** To double-confirm the authenticity, we use the separate model in **Section 3.2.1** to check whether there are multiple crosspoints. In **Fig. 4.4.2(c)**, we observe two cross points when the laser intensity is at 17.8 $mW/\mu m^2$. As a result, we successfully induce photothermal bistability in w=180 nm nanoblock by detuning the laser wavelength.

doi:10.6342/NTU202301642

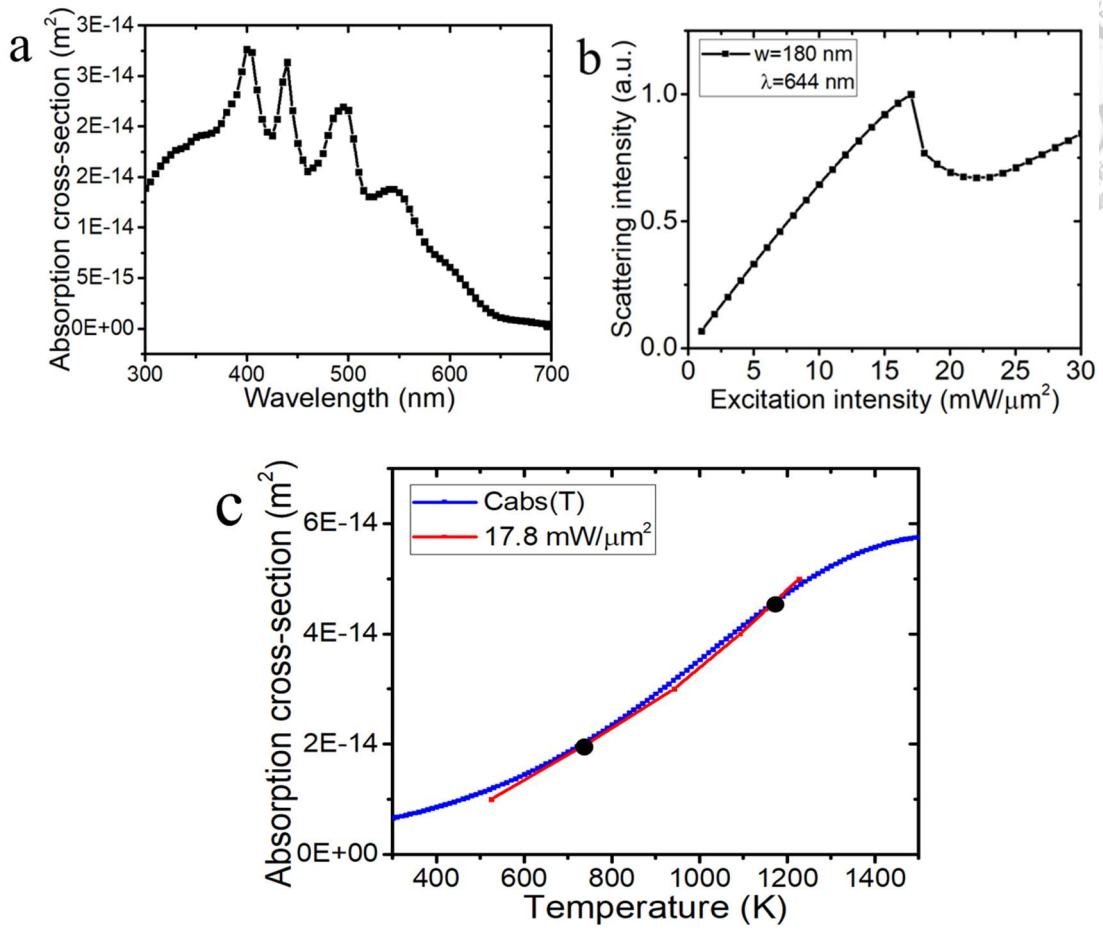

Figure 4.4.2 Photothermal bistability induced in w=180 nm nanoblock under 644 nm laser.
(a) is the absorption cross-section spectrum. The resonance peak is at around 550 nm. (b) is the intensity-dependent graph of w= 180 nm nanoblock under 644 nm laser calculated by combination model. (c) is the heat dissipation of 644 nm laser at 17.8 $mW/\mu m^2$ calculated by the separate model. The blue curve is the absorption cross section which can be regarded as the heat source. The red curve is the heat dissipation.

From the above discussion, we show the generality of size-dependent and wavelength-dependent photothermal bistability. Therefore, we can change the size of the nanoblock or detune the laser wavelength to design our desired nanostructure for application. In the next Section, we will introduce one of the applications for photothermal bistability which is resolution enhancement.

doi:10.6342/NTU202301642

4.5 Laser Scanning Images of Silicon Nanoblock by Simulation

Since we use laser scanning microscopy to observe the photothermal bistability, we are also curious about the scanning images from the simulation. We use the combination model in **Section 3.2.2** to simulate the w=110 nm nanoblock. The result is shown in **Fig. 4.5.1**. We can observe that as the excitation intensity increase, the area of the nonlinear part become larger. The reason is that when the excitation intensity increase, each position experiences more intensity. Therefore, from the excitation intensity dependence of w=110 nm nanobock in **Fig. 4.1.1(a)**, more positions transfer to the nonlinear part.

Besides, since the area of the nonlinear part increase as the excitation increase, we can also decrease the excitation intensity to get an ultra-small area of the nonlinear part. By fine-tuning the excitation intensity between 18 $mW/\mu m^2$ and 19 $mW/\mu m^2$, theoretically, we can achieve ultra-super resolution with the size of only one pixel

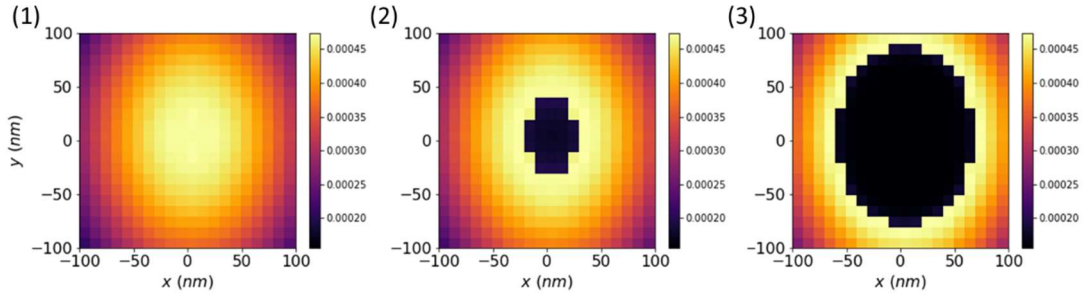

Figure 4.5.1 Simulated laser scanning images of w=110 nm nanoblock with different intensities. (1), (2), and (3) correspond to scanning images of 18 $mW/\mu m^2$, 19 $mW/\mu m^2$, and 23 $mW/\mu m^2$ respectively

doi:10.6342/NTU202301642

4.6 Observation of Photothermal Bistability from Experiment

In this section, we want to demonstrate the existence of photothermal bistability with experiments. We use the laser scanning microscopy mentioned in **Section 3.3** to obtain the scanning images of the w=110 nm silicon nanoblock with different intensities. In **Fig. 4.6.1(a)**, we examine the reversibility and repeatability of the scattering nonlinearity to ensure that the silicon nanoblock is not broken. From the figure, we observe that there is a very sharp change from the x-y profile when the scanning image is at high intensity and the shape of the nonlinear part matches well with the simulated scanning images in **Fig. 4.5.1**. In addition, we extract the scattering signal from the center of the Gaussian profile of the scanning images and plot it with excitation intensity. The experimental result of excitation intensity dependency is shown in **Fig. 4.6.1(b).**

The black and red lines are simulation result and experimental result. We can observe that the scattering intensity of both simulation and experimental results demonstrate a large nonlinearity when the intensity is around 20 $mW/\mu m^2$. The results match perfectly showing the correctness of the simulation model and the existence of photothermal bistability in crystal silicon nanoblock.

doi:10.6342/NTU202301642

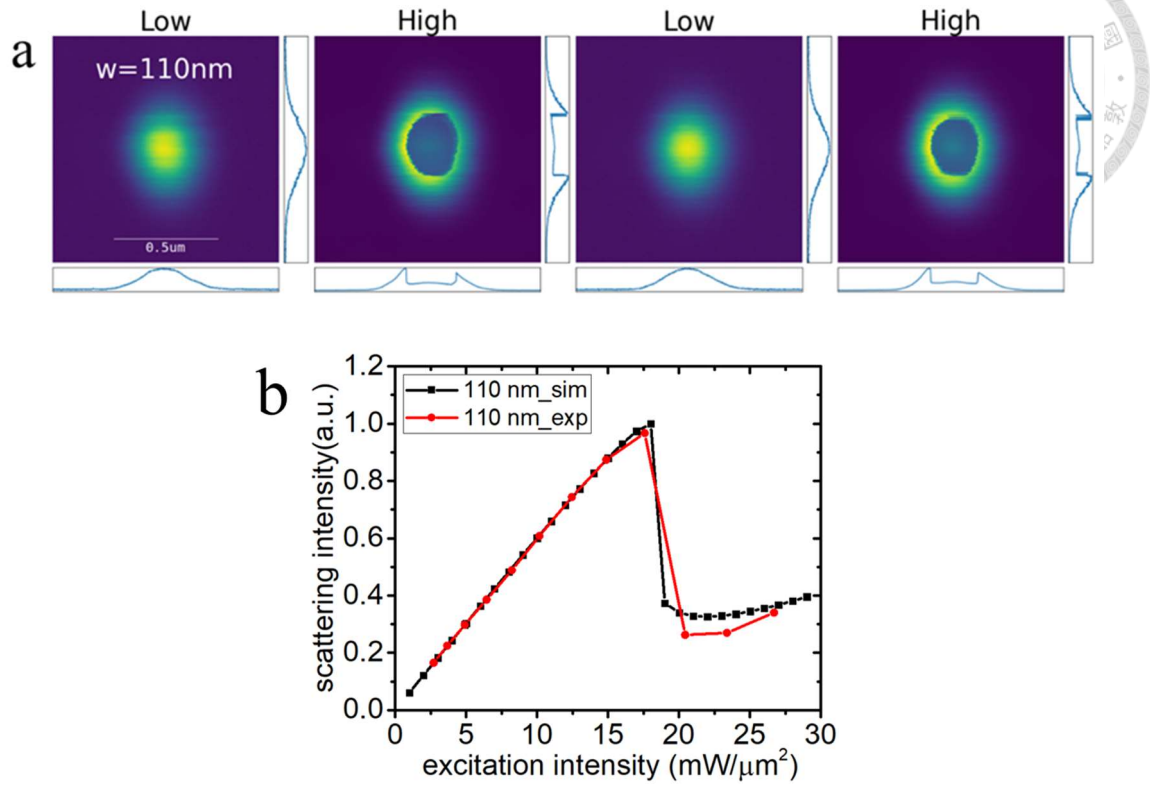

Figure 4.6.1 The scanning images and intensity dependence of w=110 nm silicon nanoblock (a)is the scanning images of low intensity 2.71 $mW/\mu m^2$ and high intensity 26.69 $mW/\mu m^2$ respectively. (Courtesy of Te-Hsin Yen) (b) is the comparison between the simulation result and experimental result for w=110 nm nanoblock. The black curve is the simulation result from the combination model and the red curve is the result of the experimental result. The red curve is Courtesy of Te-Hsin Yen.

doi:10.6342/NTU202301642

Chapter 5 Discussion and Future Work

5.1 Potential of Mapping Geometric Shape of Silicon

In **Fig. 4.6(b)**, we observe that the nonlinear part of the scanning images with w=110~150 nm forms a rectangular shape which is similar to the real shape of a nanoblock. Therefore, the nonlinear part of the scanning images may give us more information about the nanostructure. To understand the meaning of the nonlinear part, we use the simulation model in **Section 3.2.2** to simulate the laser scanning images of w=110 nm nanoblock. In **Fig. 5.1.1(a)**, we observe that scanning images show a cross shape. The reason is that when the laser scans through the nanoblock, the focal spot covers less area at the corners of the nanoblock causing less power absorption. From **Fig. 5.1.1(b)**, the white dot line is the edge of the w=110 nm nanoblock. We can see that the equilibrium temperature is smaller at the corners of the nanoblock. Since the scattering signal is sensitive to the excitation intensity from **Fig. 4.1.1(a)**, the linear signal and nonlinear signal have high contrast revealing the edge of the nanoblock. As a result, the nonlinear images of photothermal bistability may pave the way to directly observe the shape of the structure which is never done by optical microscopy.

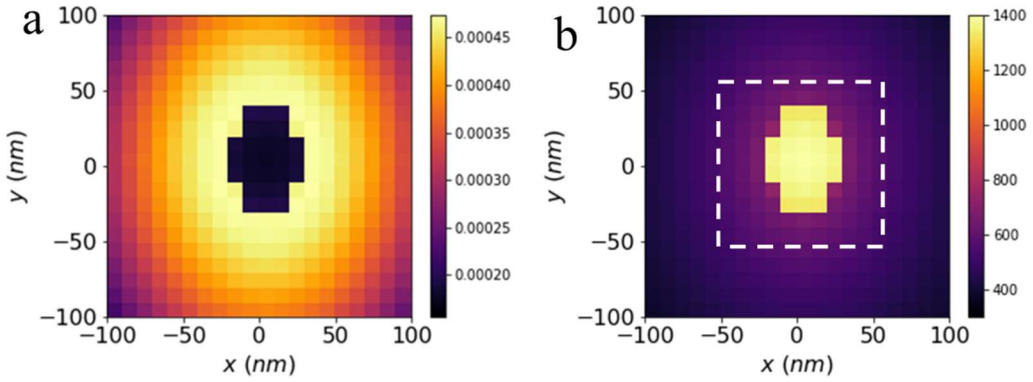

Figure 5.1.1 The scanning images of w=110 nm nanoblock at 19 $mW/\mu m^2$ from simulation.
(a) is the distribution of the scattering signal. The color bar is the magnetude of scattering intensity. (b) is temperature distribution of the w=110 nm nanoblock. The size of the nanoblock is indicated by the white dotted line, while the temperature in Kelvin is depicted by the color bar.

doi:10.6342/NTU202301642

5.2 Conclusion

In this study, we predict that w=110-150 nm silicon nanoblocks have large transition intensity dependence with photothermal bistability in **Section 4.1**. The mechanism of photothermal bistability can be explained by the nonlinearity of the temperature-dependent absorption cross-section and the cross points in **Fig. 4.1.2**. We also show the hysteresis effect of w=110 nm nanoblock and prove that the hysteresis effect comes from photothermal bistability in **Section 4.2**. In addition, we show that at the large transition intensity, the equilibrium time is microsecond scale which is four orders of magnitude higher than our previous study in **Section 4.3**. To show the generality of photothermal bistability in the nanoblock in **Section 4.4**. We show size-dependent of photothermal bistability in w=120-150 nm nanoblock. Besides, by detuning the distance between the resonance wavelength and the excitation wavelength, we can induce photothermal bistability in w= 180 nm nanoblock. Therefore, we can easily design the desired photothermal bistability device. In **Section 4.5**, we simulate the scanning images of w= 110 nm nanoblock and provide a possibility of ultra-super resolution in **Section 4.5**. In **Section 4.6**, we demonstrate a strong agreement between the experimental results and the simulation results. With the well-established simulation model and the clear physical mechanism, our study of the photothermal bistability in a low Q factor silicon nanoblock provide a guideline for designing the optimal silicon nanostructure to induce ultra-large nonlinearity.

5.3 Future Work

In the future, we would like to further study the meaning of the nonlinear images of photothermal bistability with other shapes of nanostructures as discussed in **Section 5.1**. With the example of nanoblock structure, we can design other shapes of structure with

doi:10.6342/NTU202301642

photothermal bistability. Ideally, we should be able to invent a new way to observe the shape of the nanostructure in optical microscopy.

doi:10.6342/NTU202301642

Reference

[1] X.-W. Ma *et al.*, "All-optical flip-flop based on hybrid square-rectangular bistable lasers," *Optics Letters,* vol. 42, no. 12, pp. 2291-2294, 2017.

[2] Y. D. Jeong, J. S. Cho, Y. H. Won, H. J. Lee, and H. Yoo, "All-optical flip-flop based on the bistability of injection locked Fabry-Perot laser diode," *Optics Express,* vol. 14, no. 9, pp. 4058-4063, 2006.

[3] T. Mori, Y. Yamayoshi, and H. Kawaguchi, "Low-switching-energy and high-repetition-frequency all-optical flip-flop operations of a polarization bistable vertical-cavity surface-emitting laser," *Applied Physics Letters,* vol. 88, no. 10,101102, 2006.

[4] S. John and T. Quang, "Optical bistability and phase transitions in a doped photonic band-gap material," *Physical Review A,* vol. 54, no. 5, p. 4479, 1996.

[5] Y. Wu, J. M. Ward, and S. Nic Chormaic, "Ultralow threshold green lasing and optical bistability in ZBNA (ZrF 4–BaF 2–NaF–AlF 3) microspheres," *Journal of Applied Physics,* vol. 107, no. 3,033103, 2010.

[6] C. Masoller, T. Sorrentino, M. Chevrollier, and M. Oria, "Bistability in semiconductor lasers with polarization-rotated frequency-dependent optical feedback," *IEEE Journal of Quantum Electronics,* vol. 43, no. 3, pp. 261-268, 2007.

[7] N. Brandonisio, P. Heinricht, S. Osborne, A. Amann, and S. O'Brien, "Bistability and all-optical memory in dual-mode diode lasers with time-delayed optical feedback," *IEEE Photonics Journal,* vol. 4, no. 1, pp. 95-103, 2011.

[8] G. S. He, *Nonlinear Optics and Photonics*. Oxford, 2014.

[9] M. M. Ara, E. Koushki, and H. A. Doost, "Optical bistability in TiO2 nanoparticles," *Optical Materials,* vol. 35, no. 7, pp. 1431-1435, 2013.

[10] D. Zhao, Z.-q. Wang, H. Long, K. Wang, B. Wang, and P.-x. Lu, "Optical bistability in defective photonic multilayers doped by graphene," *Optical and Quantum Electronics,* vol. 49, no. 4, pp. 1-9, 2017.

[11] V. R. Almeida and M. Lipson, "Optical bistability on a silicon chip," *Optics Letters,* vol. 29, no. 20, pp. 2387-2389, 2004.

[12] C. M. Soukoulis and M. Wegener, "Past achievements and future challenges in the development of three-dimensional photonic metamaterials," *Nature Photonics,* vol. 5, no. 9, pp. 523-530, 2011.

[13] Y. Kivshar, "All-dielectric meta-optics and non-linear nanophotonics," *National Science Review,* vol. 5, no. 2, pp. 144-158, 2018.

[14] C.-Y. Yang *et al.*, "Nonradiating silicon nanoantenna metasurfaces as narrowband absorbers," *ACS Photonics,* vol. 5, no. 7, pp. 2596-2601, 2018.

doi:10.6342/NTU202301642

[15] A. A. Nikitin *et al.*, "Carrier-induced optical bistability in the silicon micro-ring resonators under continuous wave pumping," *Optics Communications,* vol. 480,126456, 2021.

[16] P. Sun and R. M. Reano, "Low-power optical bistability in a free-standing silicon ring resonator," *Optics Letters,* vol. 35, no. 8, pp. 1124-1126, 2010.

[17] Y. Chen *et al.*, "Optical Bistability in a Tunable Gourd-Shaped Silicon Ring Resonator," *Nanomaterials,* vol. 12, no. 14, p. 2447, 2022.

[18] M. Borghi, C. Castellan, S. Signorini, A. Trenti, and L. Pavesi, "Nonlinear silicon photonics," *Journal of Optics,* vol. 19, no. 9, 093002, 2017.

[19] C. Horvath, D. Bachman, R. Indoe, and V. Van, "Photothermal nonlinearity and optical bistability in a graphene–silicon waveguide resonator," *Optics Letters,* vol. 38, no. 23, pp. 5036-5039, 2013.

[20] D. Ryabov, O. Pashina, G. Zograf, S. Makarov, and M. Petrov, "Nonlinear optical heating of all-dielectric super-cavity: efficient light-to-heat conversion through giant thermorefractive bistability," *Nanophotonics,* vol. 11, no. 17, pp. 3981–3991, 2022.

[21] I. Staude and J. Schilling, "Metamaterial-inspired silicon nanophotonics," *Nature Photonics,* vol. 11, no. 5, pp. 274-284, 2017.

[22] Y.-S. Duh *et al.*, "Giant photothermal nonlinearity in a single silicon nanostructure," *Nature communications,* vol. 11, no. 1, pp. 4101-4110, 2020.

[23] T. Zhang *et al.*, "Anapole mediated giant photothermal nonlinearity in nanostructured silicon," *Nature communications,* vol. 11, no. 1, pp. 3027-3036, 2020.

[24] G. Mie, "Beiträge zur Optik trüber Medien, speziell kolloidaler Metallösungen," *Annalen der physik,* vol. 330, no. 3, pp. 377-445, 1908.

[25] M. R. Hasan and O. G. Hellesø, "Dielectric optical nanoantennas," *Nanotechnology,* vol. 32, no. 20, 202001, 2021.

[26] A. E. Miroshnichenko, S. Flach, and Y. S. Kivshar, "Fano resonances in nanoscale structures," *Reviews of Modern Physics,* vol. 82, no. 3, pp. 2257-2298, 2010.

[27] A. E. Miroshnichenko and Y. S. Kivshar, "Fano resonances in all-dielectric oligomers," *Nano Letters,* vol. 12, no. 12, pp. 6459-6463, 2012.

[28] P. Moitra *et al.*, "Large-scale all-dielectric metamaterial perfect reflectors," *Acs Photonics,* vol. 2, no. 6, pp. 692-698, 2015.

[29] Z. Ye, X. Jiang, and Z. Wang, "Measurements of Particle Size Distribution Based on Mie Scattering Theory and Markov Chain Inversion Algorithm," *Journal of Software,* vol. 7, no. 10, pp. 2309-2316, 2012.

[30] B. J. Sumlin, W. R. Heinson, and R. K. Chakrabarty, "Retrieving the aerosol

doi:10.6342/NTU202301642

complex refractive index using PyMieScatt: A Mie computational package with visualization capabilities," *Journal of Quantitative Spectroscopy and Radiative Transfer,* vol. 205, pp. 127-134, 2018.

[31] J. Leuthold, C. Koos, and W. Freude, "Nonlinear silicon photonics," *Nature Photonics,* vol. 4, no. 8, pp. 535-544, 2010.

[32] T. V. Tsoulos and G. Tagliabue, "Self-induced thermo-optical effects in silicon and germanium dielectric nanoresonators," *Nanophotonics,* vol. 9, no. 12, pp. 3849-3861, 2020.

[33] F. Felber and J. Marburger, "Theory of nonresonant multistable optical devices," *Applied Physics Letters,* vol. 28, no. 12, pp. 731-733, 1976.

[34] M. Soljacic *et al.*, "All-optical switching using optical bistability in nonlinear photonic crystals," in *Photonic crystal materials and devices*, vol. 5000: SPIE, pp. 200-214, 2003.

[35] D. W. Pepper and J. C. Heinrich, *The Finite Element Method: Basic Concepts and Applications with MATLAB®, MAPLE, and COMSOL*. CRC Press, 2017.

[36] M. R. Hestenes and E. Stiefel, "Methods of conjugate gradients for solving," *Journal of research of the National Bureau of Standards,* vol. 49, no. 6, p. 409, 1952.

[37] J. R. Bunch and J. E. Hopcroft, "Triangular factorization and inversion by fast matrix multiplication," *Mathematics of Computation,* vol. 28, no. 125, pp. 231-236, 1974.

[38] J. Hoyland and D. Sands, "Temperature dependent refractive index of amorphous silicon determined by time-resolved reflectivity during low fluence excimer laser heating," *Journal of Applied Physics,* vol. 99, no. 6, 063516, 2006.

[39] C.-H. Li, Y.-L. Tang, J. Takahara, and S.-W. Chu, "Nonlinear heating and scattering in a single crystalline silicon nanostructure," *The Journal of Chemical Physics,* vol. 155, no. 20, 204202, 2021.

[40] 唐毓隆, "雷射掃描激發空間相依共振," 2021.

[41] T. Nagata *et al.*, "A novel Silicon-On-Quartz (SOQ) device for optical mobile applications," in *2011 International Electron Devices Meeting*, 2011: IEEE, pp. 14.1. 1-14.1. 4.

[42] Y. Nagasaki, M. Suzuki, and J. Takahara, "All-dielectric dual-color pixel with subwavelength resolution," *Nano Letters,* vol. 17, no. 12, pp. 7500-7506, 2017.

[43] R. Shankar, I. Bulu, R. Leijssen, and M. Lončar, "Study of thermally-induced optical bistability and the role of surface treatments in Si-based mid-infrared photonic crystal cavities," *Optics Express,* vol. 19, no. 24, pp. 24828-24837, 2011.

[44] M. A. Buyukkaya, C.-M. Lee, A. Mansoori, G. Balakrishnan, and E. Waks,

doi:10.6342/NTU202301642

"Low power optical bistability from quantum dots in a nanobeam photonic crystal cavity," *Applied Physics Letters,* vol. 121, no. 8, 081104, 2022.

doi:10.6342/NTU202301642